Ultrasonics - Sonochemistry 67 (2020) 105126

Contents lists available at ScienceDirect

Ultrasonics - Sonochemistry

journal homepage: www.elsevier.com/locate/ultson

Surface functionalization by nanosecond-laser texturing for controlling hydrodynamic cavitation dynamics

Martin Petkovšek[a,*], Matej Hočevar[b], Peter Gregorčič[a]

[a] Faculty of Mechanical Engineering, University of Ljubljana, Ljubljana, Slovenia
[b] Institute of Metals and Technology, Ljubljana, Slovenia

ARTICLE INFO

Keywords:
Hydrodynamic cavitation
Laser texturing
Fluid dynamics
Surface engineering
Hydrophobic/hydrophilic surface

ABSTRACT

The interaction between liquid flow and solid boundary can result in cavitation formation when the local pressure drops below vaporization threshold. The cavitation dynamics does not depend only on basic geometry, but also on surface roughness, chemistry and wettability. From application point of view, controlling cavitation in fluid flows by surface functionalization is of great importance to avoid the unwanted effects of hydrodynamic cavitation (erosion, noise and vibrations). However, it could be also used for intensification of various physical and chemical processes. In this work, the surfaces of 10-mm stainless steel cylinders are laser textured in order to demonstrate how hydrodynamic cavitation behavior can be controlled by surface modification. The surface properties are modified by using a nanosecond (10–28 ns) fiber laser (wavelength of 1060 nm). In such a way, surfaces with different topographies and wettability were produced and tested in a cavitation tunnel at different cavitation numbers (1.0–2.6). Cavitation characteristics behind functionalized cylindrical surfaces were monitored simultaneously by high-speed visualization (20,000 fps) and high frequency pressure transducers. The results clearly show that cavitation characteristics differ significantly between different micro-structured surfaces. On some surfaces incipient cavitation is delayed and cavitation extent decreased in comparison with the reference – a highly polished cylinder. It is also shown that the increased surface wettability (i.e., hydrophilicity) delays the incipient cavitation.

1. Introduction

Cavitation is initiated by the formation of vapor cavities (bubbles or voids) that grow and collapse at multiple locations and can release large density of energy in short span of time. As a physical phenomenon, it is relatively well known and has been studied intensively since the end of the 19th century on behalf of avoiding, preventing or predicting cavitation on turbomachinery. On the one hand, the hydrodynamic cavitation in fluid machinery is considered as an unwanted effect responsible for erosion, noise and vibrations that usually result in malfunction of various turbo machines [1]. In these situations, the suppression of cavitation inception is highly desired [2]. On the other hand, the hydrodynamic cavitation may also result in desired effects and can serve as advanced oxidation process, such as (waste) water treatment [3]. In this way, the cavitation offers a significant potential for the intensification of various physical and chemical processes in an energy-efficient manner [4].

Due to high importance of the hydrodynamic cavitation on different engineering applications and its significant applicability, several authors have studied how cavitation and cavitation effects can be controlled (suppressed or increased) by changing solid-body geometry [5-7] and surface properties [8-10]. However, not only the body geometry and surface properties, but also liquid characteristics, such as viscosity, vapor pressure, surface tension, dissolved gasses, and other solid impurities importantly influence cavitation dynamics and, consequently, its effects. It has been shown [11,12] that the presence of gas exponentially reduces erosion on the bulk surface, while Keller [6] empirically demonstrated the dependence of the cavitation scale effects on liquid quality and body geometry.

When hydrodynamic cavitation is developed due to increased flowrates, it goes through the following phases: *(i)* very first stage of the initial cavitation state (known also as incipient cavitation); *(ii)* the developed cavitation, which can be steady state (sheet cavitation) or oscillating (cloud cavitation) [13]; and *(iii)* the final stage (i.e.,

Abbreviations: ACA, apparent contact angle; DLT, direct laser texturing; FWHM, full width at half maximum; ROI, region of interest; IFM, infinite-focus measuring; PPA, peak-to-peak amplitude; SEM, scanning-electron microscopy

* Corresponding author.
E-mail address: martin.petkovsek@fs.uni-lj.si (M. Petkovšek).

https://doi.org/10.1016/j.ultsonch.2020.105126
Received 22 August 2019; Received in revised form 7 February 2020; Accepted 7 April 2020
Available online 10 April 2020

supercavitation), where the vapor phase overtakes a large volume of flow [14]. Since the main body geometry strongly influences on the developed and supercavitating state of cavitation, the body surface properties influence especially on incipient cavitation. Here, the surface should be considered as the outermost layer of a body that strongly influences the behavior of the interactive medium (i.e., liquid in case of cavitation) by its chemical and topographical properties.

Several authors already focused mainly on how surface topography (roughness) affects the hydrodynamic cavitation. One of the first studies on surface roughness was performed by Numachi et al. [15], where specimen profiles were prepared with various surface roughness in order to perform mutual comparison on basic cavitation characteristics. Surface roughness of profile varied within R_a = 0.05–3.2 μm. The authors reported that surface roughness advances incipient cavitation and tends to displace initial cavitation upstream. Billet et al. [16] showed, that surface roughness is an important consideration by scaling effects, where cavitation characteristics must be transferred from model to prototype geometry. One of the recent studies, where various surface roughness was compared, demonstrates that strong deviations in cavitation dynamics are formed by developed cloud cavitation [17]. Although the above-mentioned studies deal with cavitation characteristics on surfaces with various roughness, no study has been performed yet to investigate hydrodynamic cavitation on precisely defined surface topographies, induced by direct laser texturing (DLT).

Kwok et al. [18] reviewed laser surface engineering in terms of protecting materials against cavitation erosion. Various laser surface modification techniques can be used for achieving better surface resistance against cavitation erosion, such as laser transformation hardening, laser surface melting, laser surface alloying and others. These techniques were mainly used to deal with cavitation consequences, but DLT can also deal with cavitation formation and its characteristics. However, in case of DLT, the interaction between laser pulse and surface does not lead only to morphological (e.g., roughness) modifications but results also in surface chemistry modification [19-21]. This both influence surface wettability. Several studies [22-24] have shown that metallic surfaces immediately after DLT are in a (super)hydrophilic state that can be described by the saturated Wenzel regime [20,25]. But this state is not stable and hydrophobicity, or even superhydrophobicity (lotus effect) with contact angle above 150° and roll-off angles below 5° are developed if such surface is exposed to ambient conditions [22-24,26,27]. Due to this reason, the influence of the laser-textured surfaces on cavitation characteristics is much more complex as only roughness modifications, performed by conventional methods.

There are also some studies about the influence of surface wettability on cavitation behavior. In this context, Belova et al. [28,29] examined how surface hydrophilicity and hydrophobicity influence on cavitation bubbles formation, when using ultrasound induced cavitation device. Their results revealed that cavitation bubbles strongly avoid hydrophilic surfaces, which confirms that surface wettability also plays an important role by cavitation dynamics. Due to the wettability transition, DLT surfaces enable investigations of cavitation behavior on the surfaces with the same (micro) roughness, but different wettability. These aspects have not been appropriately addressed yet, although it seems that they can be used for controlling the cavitation behavior in fluid flows.

Therefore, the main aim of this work is to study, how properties of laser-textured surfaces influence on hydrodynamic cavitation dynamics, especially in initial stage by incipient cavitation. Due to this reason, we use 10-mm-long stainless-steel cylinders with diameter of 10 mm and their surfaces were modified by texturing of several patterns using a nanosecond fiber laser. The fiber laser was used since it offers a compact, robust and cost–effective approach appropriate also for industrial applications [23,30,31]. The surface wettability after laser texturing was evaluated by the apparent contact angle (ACA). Although the presented results have no ability to give an ultimate answer, how particular parameters of laser texturing influence cavitation behavior, they clearly show that this approach has significant potential for controlling cavitation and cavitation erosion. Thus, this work indicates that such an approach can offer a solution to many applications where controlling cavitation with DLT could be beneficial - from reducing cavitation aggressiveness to alleviate cavitation erosion on turbine machinery, to controlling cavitation conditions on devices designed to use cavitation phenomenon as an efficient treatment tool. Also in applications, where hydrodynamic cavitation is used as a treatment tool (water treatment [3,32], food processing [33,34], emulsion production [35,36] etc.), the erosive effects are usually not desired. Thus, it will be very useful if the negative aspects of cavitation erosion would be controlled by appropriate surface modifications.

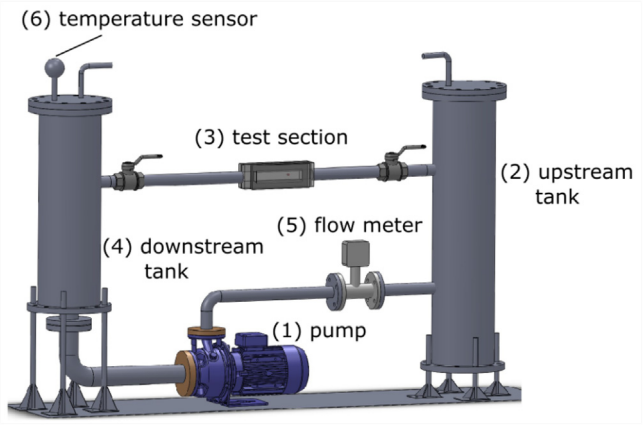

Fig. 1. Cavitation tunnel.

2. Experimental set-up

Experiments were performed in a closed loop cavitation tunnel (Fig. 1) at the Faculty of Mechanical Engineering, University of Ljubljana. Preliminary experiments were performed by Petkovšek et al. [37]. The tunnel was filled by a tap water two days before actual measurements to stabalise its temperature. During the experiments, the water temperature equaled 22 °C and did not deviate more than 2 °C. Before and after the measurements the amount of dissolved oxygen was measured with O_2 probe Intellical LDO101 on HachLange HQ430D multimeter instrument. The amount of dissolved oxygen during the experiments equalled 7.6 mg/L ± 0.2 mg/L. The cavitation tunnel and the test section are designed in a way that any uncontrolled cavitation upstream the test section is avoided.

For water circulation in cavitation tunnel a 4.5 kW pump (1) is installed. This enables the variation of rotation frequency via frequency controller to control the flow rate. The water flows through the upstream reservoir (2) into the test section (3) and through the downstream reservoir (4) back into the pump. The main purpose of the two reservoirs is to eliminate the pump pulsation and to avoid potential small bubbles to enter the test section. The upstream reservoir can also be used to raise the fluid temperature with an electric heater installed, while the downstream reservoir enables a cooling system with separated cooling loop, connected to the tap water system. Two valves are installed upstream and downstream of the test section to enable the additional control of the flow rate as well as easy and fast disconnection of the test section from the main loop. The flowrate is monitored by an electromagnetic flowmeter (5). Since the system is closed, the water level in reservoirs does not vary and the measured flow equals to the flow in the test section. Temperature of the fluid is monitored by resistance temperature detector Pt100 (6), installed into the downstream reservoir (calibrating tests confirmed that the temperature in this reservoir equals to the temperature in the test section by the accuracy ± 0.1 °C), while pressure is monitored at the inlet and outlet

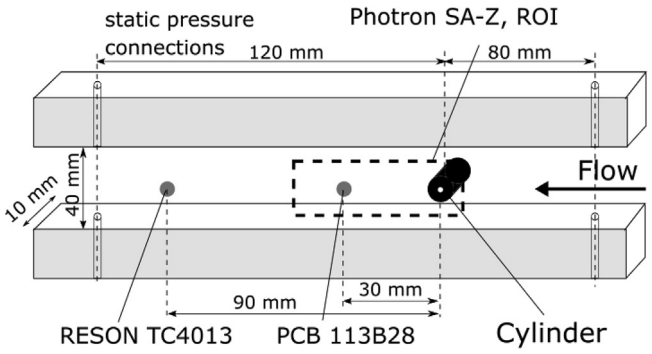

Fig. 2. Test section.

of the test section by absolute and differential pressure transducers.

The detailed description of the test section is shown in Fig. 2. It is made of a transparent acrylic glass, which enables to observe cavitation phenomena from different angles. The channel width and height equal 10 mm and 40 mm, respectively. Cavitation was observed on the 10-mm-long stainless-steel cylinders with diameter of 10 mm and modified surfaces by direct laser texturing (DLT). During the preliminary experiments, cylinders with different diameters were tested. The diameter of 10 mm was chosen to avoid influence of the bottom and top wall on the cavitation that is developed behind the cylinder, while still keeping as large cylinder surface as possible. The cylinders were installed horizontally, perpendicular to the flow direction and their centers coincident with the center of the vertical direction. They were tightly inserted into the channel from sidewall to sidewall in order to eliminate any gap between the sidewall and cylinder. Observed cavitation from the top view showed no influence due to sidewalls, since the cavitation was homogeneously distributed along the cylinder length. Static pressure was measured 80 mm upstream and 120 mm downstream from the center of the cylinder.

Experiments were performed sequentially under the same operating conditions (Table 1) for all six specimens, i.e., cylinders that are labeled S1-S6. The flowrates were chosen based on visual perception. Here, the initial flowrate (operating point B) determines the initial cavitation on the reference specimen (S1). Operating point A was added to cover the non-cavitation conditions as well. Flowrates, inlet pressures and flow temperatures were monitored and controlled, to ensure the same cavitation numbers for specific measurement points, by all specimens. First, the reference (a polished specimen) was investigated. On these measurements, the operating points were chosen based on visual perception. Then, other five modified specimens were examined.

Inlet pressure (Table 1) was measured 80 mm upstream from the center of the cylinder. Reynolds number was calculated as $Re = \frac{uL}{\nu}$, where u stands for the flow velocity at the cylinder position, L represents the distinctive length that in our case equals cylinder diameter, and ν is kinematic viscosity of the liquid. Cavitation number was determined by using the relation $\sigma = \frac{p_0 - p_v(T)}{0.5\rho u^2}$, where p_0 represents inlet pressure, $p_v(T)$ stands for the vapor pressure at the liquid's temperature, while ρ and u are the liquid's density and flow velocity at the cylinder position, respectively.

Table 1
Operating conditions.

Operating point	Flowrate (L/min)	Inlet pressure (kPa)	Reynolds number	Cavitation number
A	150	93.7	83×10^3	2.6
B	160	92.6	89×10^3	2.3
C	180	89.9	100×10^3	1.8
D	200	90.5	111×10^3	1.4
E	220	89.4	122×10^3	1.2
F	240	86.8	133×10^3	1.0

Cavitation characteristics behind circular cylinders were monitored simultaneously by high-speed visualization, high frequency pressure transducer and a hydrophone. Visualization was performed by high-speed camera Photron FastCam SA-Z at 20,000 fps and resolution of 640 × 256 pixels in 8-bit monochrome technique. Region of interest (ROI) is marked on Fig. 2 by the dashed rectangular. ROI area equaled 59.3 × 23.7 mm^2. High power LED illumination allowed to set shutter time down to 1.25 μs, at medium opened aperture. Pressure oscillations were measured 30 mm downstream by PCB 113B28 pressure transducer and hydrophone RESON TC4013, 90 mm downstream at 500 kHz each, via National Instrument cDAQ 9222 measurement card. The PCB pressure transducer was used for the verification reasons (see Figs. S23 and S24 in Supporting Information). Both, pressure transducer and hydrophone were mounted directly on the side wall of the test section with the recessed installation in order to protect the sensor's diaphragm from cavitation erosion. High-speed camera and National Instruments measurement card were triggered simultaneously by an external trigger.

2.1. Surface texturing

As a reference sample, we used a highly-polished surface (S1). Additionally, we prepared four different DLT samples (S2-S5). They were textured by using a fiber laser (SPI Lasers, Ltd., G4, SP-020P-A-HS-S-A-Y), radiating pulses with a wavelength of 1060 nm and with variable pulse duration. The cylinders were mounted on the rotational stage with an angular resolution of 0.005° in a way that their symmetrical axis was aligned with the stage axis of the rotation. The top part of the cylinder surface was placed into the focus of an F-theta lens with a focal length of 163 mm (see Supplementary Fig. S1). The beam spot size (i.e., the beam waist diameter) on the surface equaled 38 μm. A scanning head (Raylase GmbH, SS-IIE-10) was used to deliver laser pulses along the top surface of the cylinder in the x direction, parallel to the symmetrical axis of the cylinder.

We have chosen the following processing parameters to texture four different samples (details of processing parameters are collected in Supplementary Table S1):

- *Dimpled sample (S2)* was processed by drilling the holes in a hexagonal arrangement. The distance between the hole's centers equaled 130 μm. The laser pulses were 10 ns long (Full Width at Half Maximum, FWHM) and average power equaled 19 W. The pulse repetition rate equaled 900 kHz, while each hole was drilled for 30 ms, resulting in 27,000 pulses.
- *Velvet sample (S3)* was textured by high overlapping of successive microchannels. Each microchannel was processed by one pass in the x direction with scanning velocity of 540 mm/s, pulse duration (FWHM) of 28 ns, pulse frequency 90 kHz and average power of 19 W. After each scan, the sample was rotated by an angle $\Delta\varphi = 0.13°$. Therefore, the distance between two scanning lines equals $\Delta y = 11$ μm.
- *Oxidized sample (S4)* was textured by using 10-ns-long pulses, pulse frequency of 100 kHz and average power of 3.7 W. Each line was processed by scanning velocity of 300 mm/s and the high overlapping of successive lines was achieved by small angle step of $\Delta\varphi = 0.01°$ that equals to scan line separation of $\Delta y = 0.9$ μm.
- *Waved sample (S5)* was processed by pulses of 28 ns, pulse frequency of 90 kHz, scanning velocity of 540 mm/s and average power of 19 W. The angle step of $\Delta\varphi = 0.77°$ resulted in scanning line separation of $\Delta y = 67$ μm.
- *Grooved sample (S6)* was textured by microchannels that were separated by $\Delta y = 130$ μm. Each channel was drilled by 10 passes of a laser beam across the x direction with scanning velocity of 540 mm/s. The same scanning speed, pulse duration and pulse frequency as in sample S5 was used.

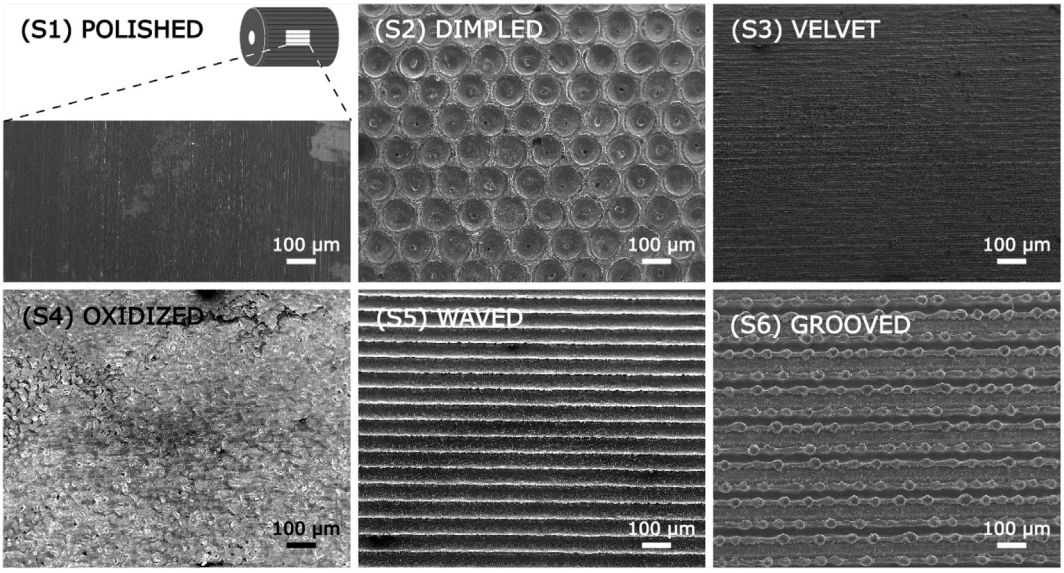

Fig. 3. SEM images of surfaces of the polished (reference) and the laser-textured cylinders.

3. Results and discussion

3.1. Surface morphology

Surface morphology is revealed by using scanning electron microscope (SEM) and 3D optical Infinite-Focus Measuring (IFM) device. SEM images are shown in Fig. 3 (see also Supplementary Figs. S2–S10 for higher magnifications SEM images and SEM images acquired in tilted mode). The 3D surface structures are presented in Fig. 4 and the surface parameters are summarized in Table 2. The peak-to-peak amplitude (PPA) presents an average height between the valley and the peak over a profile curve, as schematically shown in Supplementary Fig. S12.

The surface roughness is evaluated by the average height of the selected area, i.e., the S_a parameter (see Eq. (S7) in Supporting Information). To enable better comparison with other (existing and future) studies, the roughness of a profile R_a is also provided in Table 2 and the methodology of its evaluation is revealed in Supporting Information. The reference, polished surface has surface roughness $S_a = 0.44 \pm 0.01$ µm that increases by laser texturing, as expected. In case of dimpled surface, each hole was drilled by 27,000 pulses resulting in total energy of 0.57 J per spot. In this way, we textured the surfaces by holes having a diameter of 110 µm and forming a hexagonal pattern with center-to-center distance of 130 µm. Average PPA of the holes equals 26 ± 4 µm (see also Profile curve in Supplementary Fig. S12).

Table 2
Surface parameters: Peak-to-peak values, average height of selected area S_a and roughness of a profile R_a for the tested samples.

Sample	Peak-to-peak value [µm]	S_a [µm]	R_a [µm]
Reference (S1)	/	0.44 ± 0.01	0.37 ± 0.01
Dimpled (S2)	26 ± 4	6.2 ± 0.1	6.6 ± 0.3
Velvet (S3)	4.3 ± 1.4	1.0 ± 0.03	1.0 ± 0.03
Oxidized (S4)	/	0.54 ± 0.05	0.55 ± 0.08
Waved (S5)	10.5 ± 1.5	2.9 ± 0.1	3.0 ± 0.04
Grooved (S6)	58 ± 1.5	18.3 ± 0.3	18.4 ± 0.5

Samples S3-S6 were textured by leading the laser beam over parallel lines separated by different distances Δy. The oxidized surface was processed by the lowest pulse fluence of 3.3 J cm^{-2}. Thus, its morphology on a microscopic level has not significantly changed due to laser texturing. Its surface roughness ($S_a = 0.54 \pm 0.05$ µm) is just slightly higher as in case of the reference surface and the profile curve does not express significant periodicity (Supplementary Fig. S14). Instead, a thin layer of oxide formed over the whole surface. On contrarily, higher pulse fluence was used for producing the velvet and the waved surface morphologies. These surfaces were textured by the same

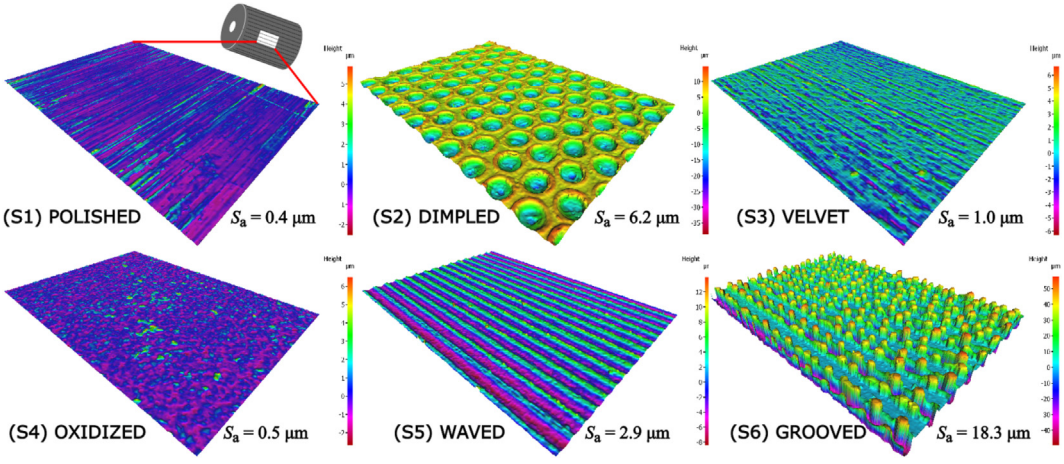

Fig. 4. 3D morphology of the surfaces of the cylinders used in the experiments.

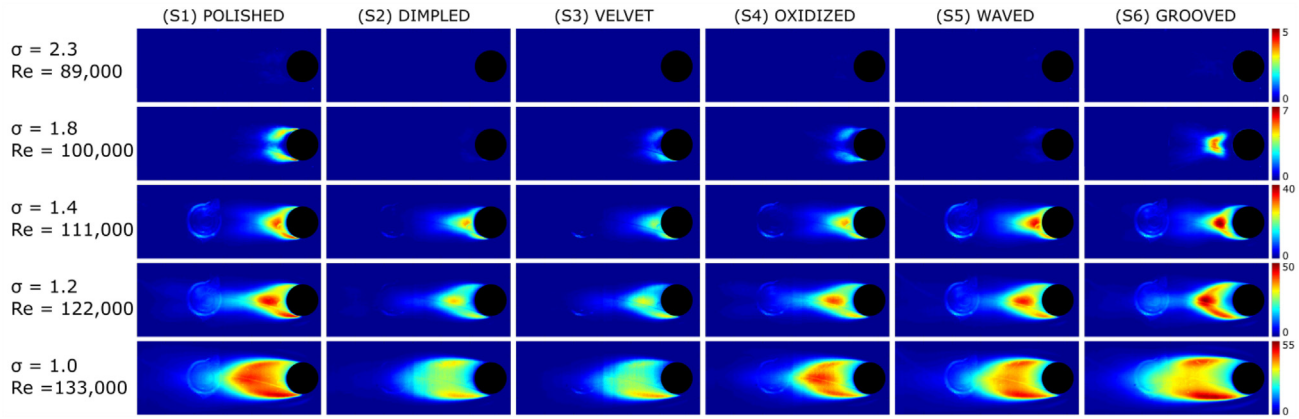

Fig. 5. Mean value of the gray level distribution of cavitation images.

processing parameters (including pulse fluence), but with different scanning line separation. As shown before [20,38], decreasing the scanning line separation significantly below the width of microchannels results in decreased surface roughness. Due to this reason, the surface roughness S_a decreases from 2.9 ± 0.1 μm (for the waved surface) to 1.0 ± 0.03 μm (for the velvet surface), while the PPA decreases from 10.5 ± 1.5 μm to 4.3 ± 1.4 μm (see also Supplementary Figs. S11–S16).

The grooved surface was produced by the same pulse fluence as the velvet and waved surfaces, but each microchannel was drilled by 10 passes of the laser radiation over the same line. This results in 58 ± 1.5 μm deep and 45-μm wide microchannels that are separated by 130 μm. The edges experienced a significant increase in height due to the remolten material during the processing (see also Supplementary Fig. S16).

3.2. Cavitation dynamics

The size and the intensity of the hydrodynamic cavitation for all six specimens at all five operating conditions (B-F) are visualized by the mean value of the gray level distribution of cavitation (Fig. 5) and by the standard deviation for this distribution (Fig. 6). Operating condition A is omitted from Figs. 5 and 6, due to absence of cavitation. Time resolved images of cavitation behind the specimens are presented on Supplementary Figs. S17–S21.

The used visualization method requires the two-phase flow, since the image appears due to light scattering on the cavitation bubbles (representing the fluid-gas interface). The mean value and the standard deviation of the gray level distribution is calculated from $N = 10{,}000$ visualization images (an acquisition period of 0.5 s) in a monochrome technique and saved with 8-bit grayscale color depth, similarly as already described in Ref. [39]. In Fig. 5, the mean value for the j^{th} pixel is calculated as

$$\langle I(j)\rangle = \frac{\sum_{i=1}^{N} I_i(j)}{N}, \tag{1}$$

where index i corresponds to particular image. A single pixel intensity $I_i(j)$ in 8-bit grayscale can take an integer value between 0 and 255 and each image contains 640 × 256 pixels, so $j = 1, \ldots, 163{,}840$.

To improve the image perception, color bars are used in Fig. 5. Here, the blue color corresponds to value 0 (no cavitation appeared at the selected pixel within all the analyzed images), while the red color presents the highest average values. The void fraction can only be qualitatively estimated via visualization. However, one must be aware, that color scales differ between operating points (B-F) to maximize the image contrast. The same color scales are used for all the samples at the same operating condition.

Fig. 6 shows calculated standard deviations of the gray level distribution of the cavitation, calculated as

$$\delta_{I(j)} = \sqrt{\frac{\sum_{i=1}^{N} (\langle I(j)\rangle - \langle I_i(j)\rangle)^2}{(N-1)}} \tag{2}$$

Similar as in Fig. 5, the color bars were used. Here, the blue color corresponds to standard deviation 0, while the red color indicates the highest standard deviation. Again, color scales differ between operating points, but are the same between various samples at a single operating condition.

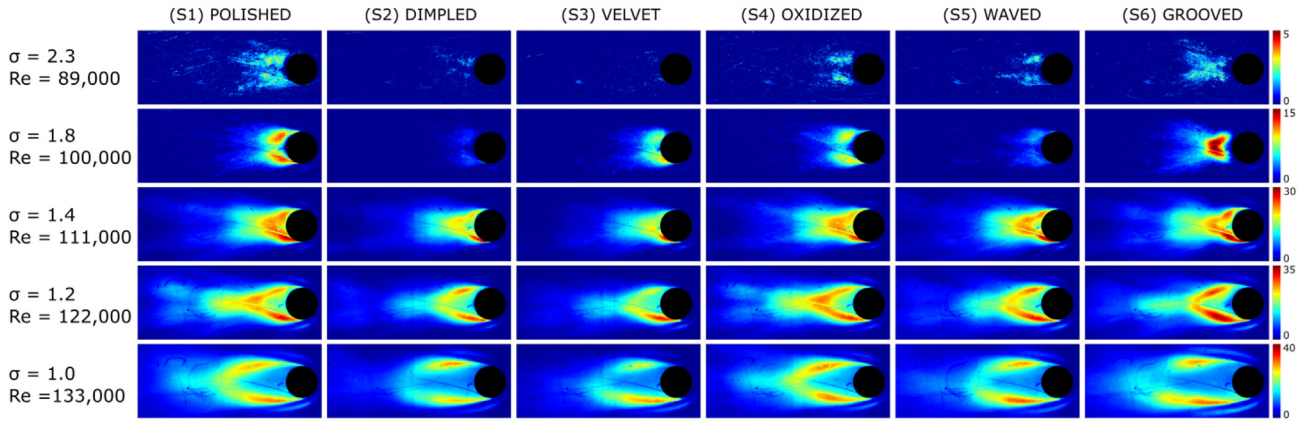

Fig. 6. Standard deviation of the gray level distribution of cavitation images.

Operating condition at $\sigma = 2.3$ was chosen with polished sample (S1), where cavitation was not yet visible by a naked eye, but already audio perceived. In Fig. 5, only slight deviation in average gray level distribution can be noticed, while in Fig. 6, sufficient change in the gray level distribution can be seen to confirm the presence of cavitation. Comparing other five samples (S2 – S6) with S1 is showing that incipient cavitation appears first on the sample S1, while S3 and S2 seem to have better "resistance" against incipient cavitation. By increasing the Reynolds number (decreasing the cavitation number) the cavitation extent increases by all the samples. Comparing different samples between each other, one can notice, that average cavitation extents differ, since differences in shape and intensity can be observed from the gray level distribution.

Comparison of the cavitation distribution between the laser textured samples of different roughness and the reference sample S1 in Fig. 5 reveals the following:

- Laser texturing delays the incipient cavitation and slightly reduces the cavitation intensity at lower cavitation numbers, which is visible from the comparison between the polished sample S1 and the oxidized sample S4 (having the surface roughness S_a similar as the sample S1) as well as by the sample S3 with just slightly higher surface roughness.
- When the surface roughness is further increased, as in the samples S2, the cavitation incipience is further delayed and the cavitation intensity at higher numbers is further decreased. In this context, the samples S2 and S5 act very similar at cavitation numbers $\sigma = 2.3$ and $\sigma = 1.8$. Here, the incipient cavitation is present in smallest intensity and extent in comparison with all other samples. However, the cavitation behind the dimpled sample S2 is strongly suppressed even by all other operating conditions. Cavitation intensity behind the waved sample S5 at lower cavitation numbers (between $\sigma = 1.4$ and $\sigma = 1.0$) is only minor decreased in comparison with the polished sample S1.
- As would be expected, significant increase of the surface roughness gains the cavitation intensity. Thus, the sample S6 with the highest surface roughness $S_a = 18.3 \pm 0.1$ μm causes the biggest cavitation extent by the lowest cavitation number, and cavitation dynamics is clearly changed (e.g., see Figs. 5 and 6 at cavitation number $\sigma = 1.8$).

Fig. 7 shows the average cavitation length behind the reference and the five laser-textured samples. Cavitation length was measured from the center of the cylinder to the position, where the normalized gray level intensity equals 0.5, as described in details in Supporting Information (Figs. S22, S23 and Table S2). It is clearly seen that the longest cavitation at all five Reynolds numbers appears behind the grooved specimen, while the velvet and dimpled specimens lead to the smallest cavitation extent.

Fig. 8 shows the frequency spectra, measured by a hydrophone 90 mm downstream from the cylinder. Inspecting pressure analysis, one can notice two distinctive parts on the pressure frequency diagrams. Primary peaks appear below 500 Hz, while the secondary peaks are visible at higher frequencies. The secondary peaks are related to cavitation (at non-cavitating conditions they are not present), while the primary peaks most probably present frequencies caused by the von Karman vortex street at non-cavitating conditions. It is, however, not excluded that part of the primary frequency spectra is related to the cavitation tunnel operation noise (the pressure pulsations from the circulation pump or the electric noise).

Fig. 8 presents the frequency spectra at the following selected cavitation numbers for all six specimens:

- non-cavitating conditions ($\sigma = 2.6$);
- the beginning of the developed cavitation ($\sigma = 1.8$);
- the developed cavitating conditions ($\sigma = 1.4$); and
- the fully developed cavitating conditions ($\sigma = 1.0$), which appears on the boundary of the supercavitation.

Comparison between the pressure analysis (Fig. 8) and the visualization (Figs. 5 and 6) reveals fine correlations. This correlation is also confirmed by the comparison of the frequency spectra, measured by the hydrophone and calculated from the acquired images in Fig. S24 (Supporting Information). At cavitation number 1.8, the cavitation is well developed on the polished and the grooved sample (Fig. 5). This is clearly noticed also on the frequency spectra on Fig. 8. By the other four samples (dimpled, velvet, oxidized and waved), the secondary peaks in the frequency spectra at this flow rate are very weak. This corresponds well with the observed small-scale cavitation during the visualization.

At cavitation number 1.4, a very distinctive peak is rising at frequency of 500 Hz for almost all the samples, with an exception of the grooved sample having this peak at about 10 Hz lower frequency. This peak is a consequence of cavitation cloud shedding, in shape of the von Karman street vortex. This is additionally confirmed by the frequency analysis of the acquired images (see Fig. S24 in Supporting Information). Overall cavitation dynamics behind various samples differ between cavitation numbers 2.3 and 1.0. Surface finishing strongly affects the cavitation development at its initial stages.

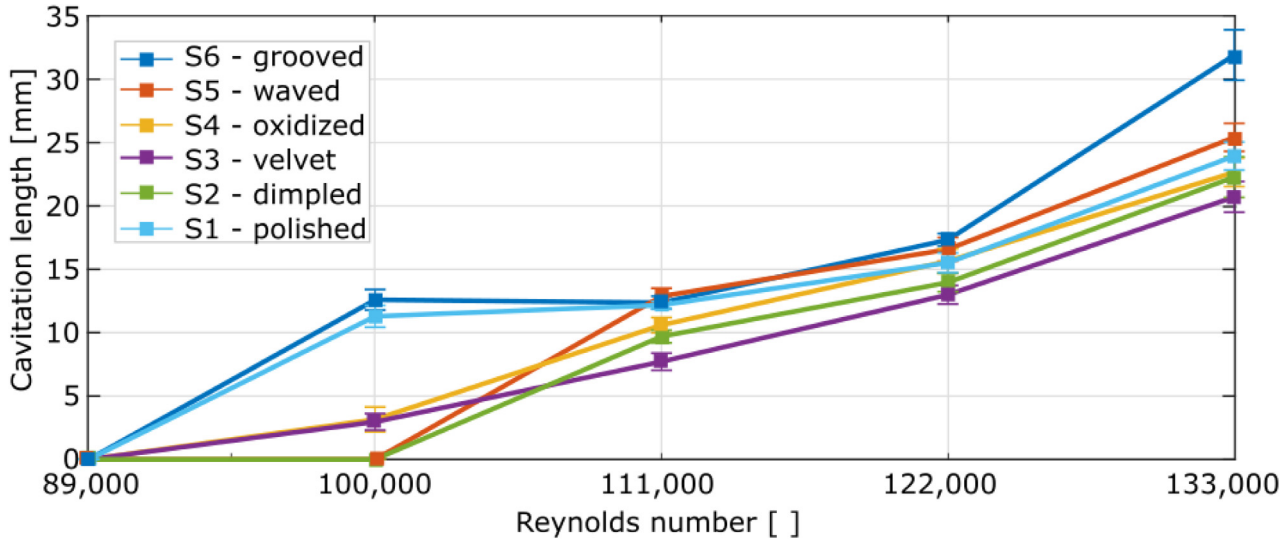

Fig. 7. Average cavitation length behind various laser textured specimens.

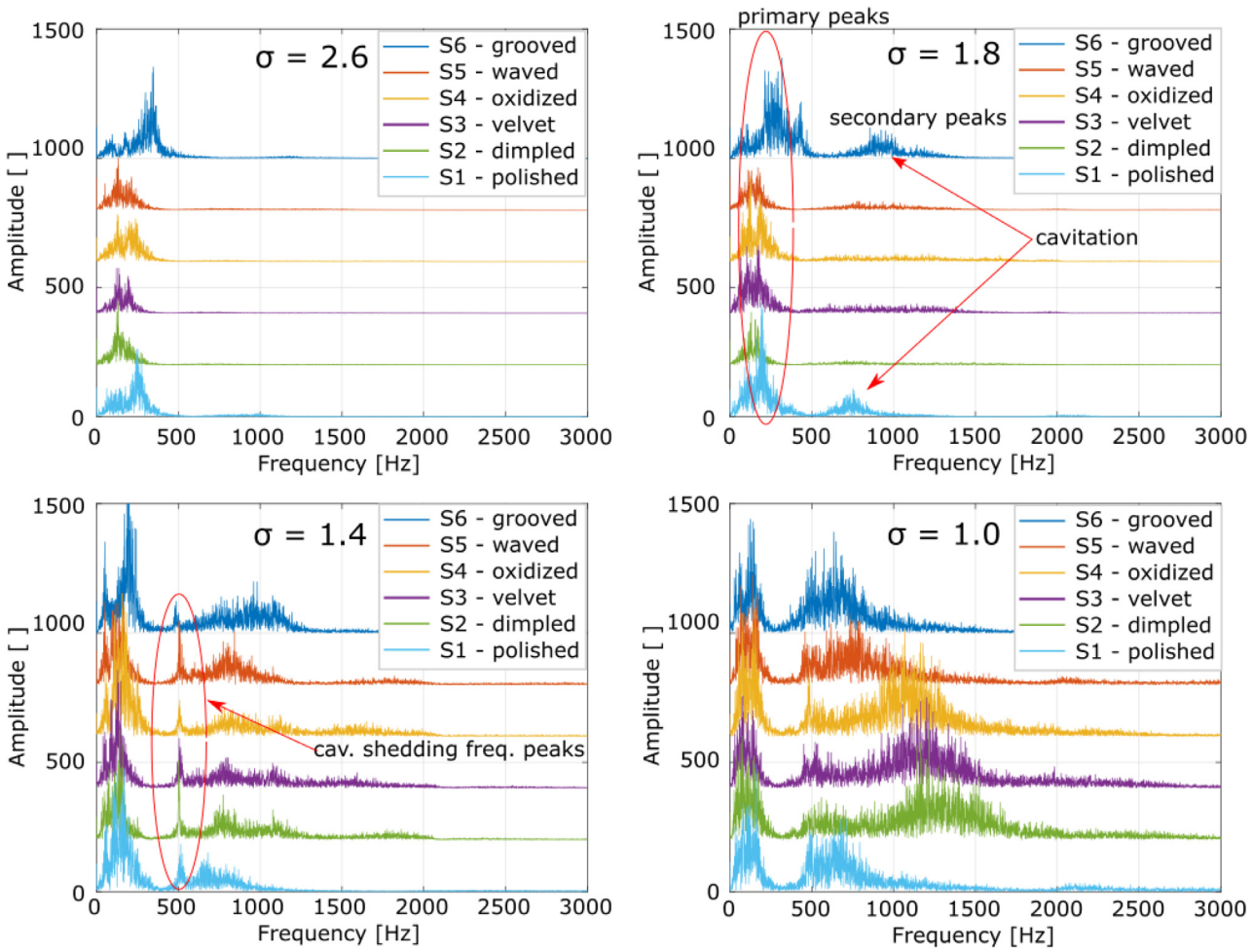

Fig. 8. Frequency spectra for all six samples at four operating conditions (σ = 2.6, σ = 1.8, σ = 1.4 and σ = 1.0).

Furthermore, it also influences on the developed cavitation regimes (Figs. 7, 8). This reflects in cavitation length (Fig. 7), cavitation shape (Fig. 5) and shedding dynamics (Figs. 6, 8).

The cavitation behavior of the tested sample via pressure analysis was quantified by a dimensionless Strouhal number *St*, defined as:

$$St = \frac{f_0 L}{u} \tag{3}$$

In Eq. (3), f_0 stands for the shading frequency, L represents the distinctive length which in our case equals to the cylinder diameter, while u stands for the freestream flow velocity.

The primary frequency peaks in Fig. 8 only slightly vary by sample to sample, while the secondary peaks, representing the cavitation activity, significantly differentiate by samples. The individual peak frequencies f_0 were determined from the measured frequency spectra by fitting the Gaussian function to the secondary frequency peaks (see Fig. S26 and Eq. (S14) in Supporting Information). Similarly, the standard deviation of the Strouhal number was calculated from the spectral width of the secondary peaks (e.g., see σ_f in Fig. S26 in Supporting Information). The representative Strouhal numbers and amplitudes as a function of the Reynolds number are shown in Fig. 9 (the numerical values are listed in Supporting Table S2). The comparison of the frequency peaks for all six samples at individual operating condition clearly indicates that the surface properties influence the cavitation response.

The central frequency of the secondary peak generally decreases with the cavitation growth. This correlates well with the visualization revealing that increasing cavitation extent leads to longer oscillating times of cavitation (lower shedding frequencies). As clearly visible from Fig. 8, the operating point with the highest Reynolds number results in intense frequency increase at three modified samples (dimpled, velvet, oxidized). The visualization suggests that this happens due to the shedding parts of cavitation clouds from the main cavitation structure - the classic von Karman street is not formed. On contrarily, cavitation on the polished and the grooved samples seems to still preserve the von Karman street vortex shedding. The amplitudes of the secondary frequency peaks generally increase with the Reynolds number or cavitation increase.

As visible from Fig. 9, the difference between the sample surfaces leads to different trends in amplitudes of the secondary frequency peak as a function of the Reynolds number. The polished, waved and grooved samples reach the amplitude peak at cavitation number σ = 1.2, while the amplitude for the dimpled, velvet and oxidized samples monotonically increase up to the cavitation number 1.0. However, they most probably reach the amplitude peak at lower cavitation numbers, not considered in this study. When the supercavitation state is developed, the cavitation oscillations and aggressiveness start to decrease due to cavity-cavity interference or the so-called cushioning effect [12]. The presented results show that for specific surface modifications (dimpled, velvet and oxidized) pressure pulsations (parameter related to the cavitation aggressiveness) can be decreased in comparison with the polished sample.

3.3. Influence of the surface wettability

Another aspect of the laser-textured metallic surfaces is their ability

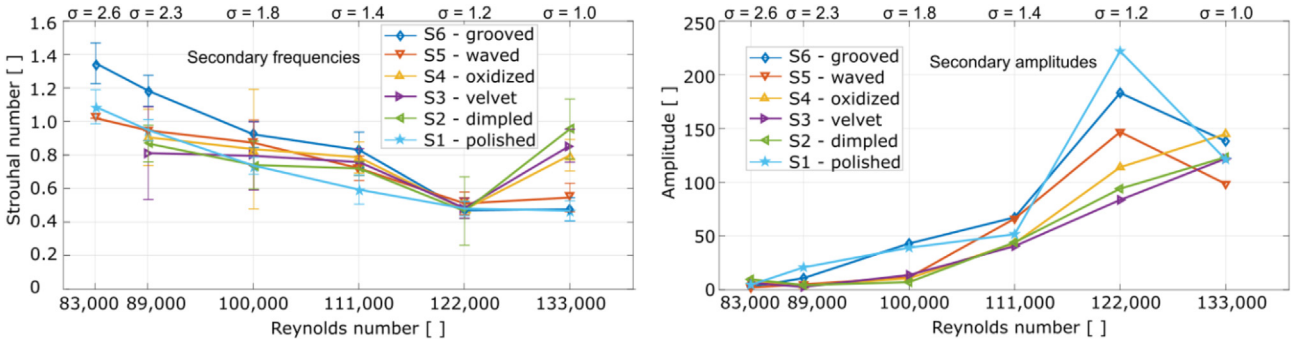

Fig. 9. Representative Strouhal numbers and amplitudes depending on Reynolds number for all six specimens by pressure measurements.

to develop hydrophobicity while keeping their micro-meter topography [40]. It is well-known that metallic surfaces immediately after the laser texturing are in a (super)hydrophilic Wenzel state [20,25,40]. However, this state is not stable and hydrophobicity, or even superhydrophobicity (lotus effect) with contact angle above 150° and the roll-off angles below 5° are developed if such a surface is exposed to ambient conditions [20,22,23]. We used this intrinsic property of the laser-textured surfaces to study the influence of wettability on the cavitation behavior. In this context, we performed the experiments by using the following three different samples that were stored in atmospheric air:

- the reference (S1, non-laser textured) sample with an apparent contact angle (ACA) of 90°;
- the oxidized sample (S4) two weeks after the laser texturing, when the ACA of 141° was developed; and
- the oxidized sample (S4.1) one week after the laser texturing, when the ACA equaled 51°.

The oxidized sample (S4) was chosen since its surface roughness is very similar to the surface roughness of the reference sample (see Table 2). Their contact angles before and after the cavitation-dynamics experiments are shown in Fig. 10 (a). In such a way, we were able to directly compare the influence of wettability on the cavitation dynamics by excluding any significant influence of micro topography. The results are presented in Fig. 10.

Fig. 10(b) showing the average cavitation extent on the tested samples at four different cavitation numbers reveal significant influence of wettability on the cavitation dynamics. From these results (samples S4 and S4.1), it seems that increased wettability (lower ACA) delays the incipient cavitation. In case of hydrophilic surface, the liquid tends to stay in a contact with surface, thus it breaks or separates from the surface at higher energies. This acts like an initial cavitation delay.

Comparison of the ACA between the samples, before and after the cavitation experiments [Fig. 10(a)] reveals that ACA by the polished sample did not change and remained 90°. However, the contact angle in case of the hydrophobic laser-textured surface decreases after these experiments. This might happen, since the development of the water repellency on the laser-textured metallic surfaces is most probably related by the absorption of hydrocarbon contaminants from the atmosphere, where the processed samples are stored [41–43]. This contamination may be partially removed during cavitation.

4. Conclusions

In this study, we have used different laser processing parameters to texture five various surface topographies (dimpled, velvet, oxidized, waved and grooved). They were used in fluid flow inducing cavitation and the results were compared to a reference, i.e., highly polished surface. Best reduction results by means of cavitation extent and its pressure oscillations were achieved at the velvet, dimpled and oxidized surface topographies. The results prove that cavitation characteristics significantly depend not only on the surface roughness, but also on the surface wettability. The increased wettability (lower apparent contact angles) delays the incipient cavitation, since the liquid tends to stay in a contact with the hydrophilic surface. Thus, the liquid separates from the surface at higher flowrates (representing higher energies). Here, the development of the surface wettability on the laser-textured metallic surfaces by time offers an interesting approach to test the interaction between the fluid flow and the curved surfaces with the same micro-topography, but different wettability.

The presented results clearly demonstrate that cavitation on the same basic geometry (cylinder) can be efficiently controlled by *laser surface engineering*. If appropriate laser-texturing parameters are used, cavitation can be decreased, or initial cavitation can be shifted to lower cavitation numbers. The visual observation and pressure measurements endorse the direct laser texturing as a potential technique for controlling cavitation dynamics. Thus, laser surface engineering is proven as a promising tool for modification of the surface properties leading to: *(i) reduced* risk of cavitation to appear or eventually reduced cavitation

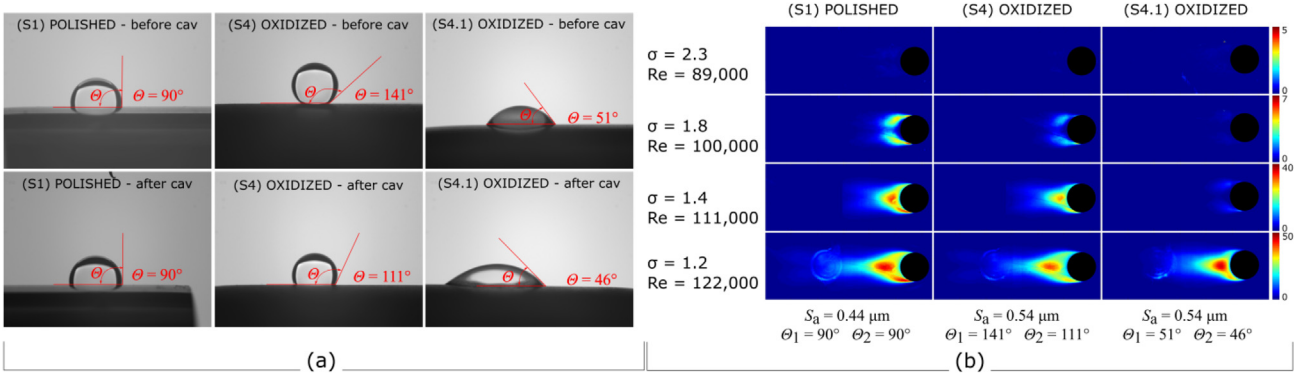

Fig. 10. (a) Apparent contact angles at the tested surfaces before and after the cavitation experiments. (b) Average cavitation extent on the tested samples.

extent or its aggressiveness and, consequently, the cavitation erosion; and *(ii) increased* cavitation effects, when needed for, e.g., advanced oxidation processes. However, further investigation is still needed to understand the fundamental underlying mechanisms. Here, examination of the single-phase flow on the laser-textured surfaces, e.g., by using particle image velocimetry, may clarify the distinctive influence of the surface topography and wettability on the cavitation incipience.

Author contributions

P.G. designed, developed and performed laser-induced surface modifications on tested samples. M.P. designed and performed the experiments in cavitation tunnel, as well as analyzed and evaluated visualization and pressure signals. M.H. performed surface characterization. M.P. and P.G. contributed to the writing of the manuscript. All authors contributed to the interpretation of the results. P.G. accepted the role of the leading author and conducted the research connected with surface engineering, laser texturing, surface characterization and interpretation of the chemical and topographical surface modifications. All authors have approved the final version of the manuscript.

6. Funding sources

This research was funded by Slovenian Research Agency (Program Nos. P2-0401, P2-0392, P2-0132, and Project Nos. Z2-8188, J7-1814, Z2-9215, J2-1741).

Decalaration of Competing Interest

The authors declare no competing financial interest.

Acknowledgements

The authors acknowledge the financial support from the Slovenian Research Agency (research core funding No. P2-0401, P2-0392, P2-0132 and projects No. Z2-8188, J7-1814, Z2-9215, J2-1741). The authors would also like to thank SPI Lasers Ltd. for their support by loan of their fiber laser within the research project *Surface functionalization by nanosecond fiber laser texturing (nsFLaT)*.

Appendix A. Supplementary data

Supplementary data to this article can be found online at https://doi.org/10.1016/j.ultsonch.2020.105126.

References

[1] A. Ferrari, Fluid dynamics of acoustic and hydrodynamic cavitation in hydraulic power systems, Proc. R. Soc. A Math. Phys. Eng. Sci. 473 (2017) 20160345, https://doi.org/10.1098/rspa.2016.0345.
[2] R.E.A. Arndt, Cavitation in fluid machinery and hydraulic structures, Annu. Rev. Fluid Mech. 13 (1981) 273–326, https://doi.org/10.1146/annurev.fl.13.010181.001421.
[3] M. Dular, T. Griessler-Bulc, I. Gutierrez-Aguirre, E. Heath, T. Kosjek, A. Krivograd Klemenčič, M. Oder, M. Petkovšek, N. Rački, M. Ravnikar, A. Šarc, B. Širok, M. Zupanc, M. Žitnik, B. Kompare, Use of hydrodynamic cavitation in (waste)water treatment, Ultrason. Sonochem. 29 (2016) 577–588. DOi:10.1016/j.ultsonch.2015.10.010.
[4] P.R. Gogate, A.M. Kabadi, A review of applications of cavitation in biochemical engineering/biotechnology, Biochem. Eng. J. 44 (2009) 60–72, https://doi.org/10.1016/j.bej.2008.10.006.
[5] M. Dular, I. Khlifa, S. Fuzier, M. Adama Maiga, O. Coutier-Delgosha, Scale effect on unsteady cloud cavitation, Exp. Fluids 53 (2012) 1233–1250.
[6] A.P. Keller, Cavitation Scale Effects Empirically Found Relations and the Correlation of Cavitation Number and Hydrodynamic Coefficients, Cav2001. (2001) 1–18. https://resolver.caltech.edu/CAV2001:lecture.001 (accessed January 12, 2020).
[7] E. Amromin, Computation of cavitation inception numbers for 3D surface irregularities, Appl. Ocean Res. 70 (2018) 54–61, https://doi.org/10.1016/J.APOR.2017.12.002.
[8] J. Fahim, S.M.M. Hadavi, H. Ghayour, S.A. Hassanzadeh Tabrizi, Cavitation erosion behavior of super-hydrophobic coatings on Al5083 marine aluminum alloy, Wear. 424–425 (2019) 122–132. DOI:10.1016/J.WEAR.2019.02.017.
[9] Y. Li, Y. Lian, Y. Sun, Cavitation erosion behavior of friction stir processed nickel aluminum bronze, J. Alloys Compd. 795 (2019) 233–240, https://doi.org/10.1016/J.JALLCOM.2019.04.302.
[10] M. Williams, E. Kawakami, E. Amromin, R.E. a Arndt, Effects of surface characteristics on hydrofoil cavitation (CAV2009 - Paper No. 112), 7th Int. Symp. Cavitation. (2009) 6 pages. http://home.safl.umn.edu/bmackay/pub/techpapers/A/tp_2009-030a.pdf.
[11] M. Dular, B. Širok, B. Stoffel, The influence of the gas content of water and the flow velocity on cavitation erosion aggressiveness, J. Mech. Eng. 51 (2005) 132–145.
[12] J.G. Auret, O.F.R.A. Damm, G.J. Wright, F.P.A. Robinson, The influence of water air content on cavitation erosion in distilled water, Tribol. Int. 26 (1993) 431–433, https://doi.org/10.1016/0301-679X(93)90083-D.
[13] X. Wu, E. Maheux, G.L. Chahine, An experimental study of sheet to cloud cavitation, Exp. Therm. Fluid Sci. 83 (2017) 129–140, https://doi.org/10.1016/j.expthermflusci.2017.01.004.
[14] J.P. Franc, J.M. Michel, Fundamentals of Cavitation, Kluwer Academic Publishers, 2004.
[15] F. Numachi, Effect of surface roughness on cavitation performance of hydrofoils—report 3, J. Basic Eng. 89 (1965) 201, https://doi.org/10.1115/1.3609554.
[16] M.L. Billet, J.W. H, B.R. Parkinf, Scale Effects on Cavitating Flows Due to Surface Roughness and Laminar Separation, AIAA J. 20 (1982) 632–637. DOI:10.2514/3.7935.
[17] J. Hao, M. Zhang, X. Huang, The influence of surface roughness on cloud cavitation flow around hydrofoils, Acta Mech. Sin. Xuebao 34 (2018) 10–21, https://doi.org/10.1007/s10409-017-0689-0.
[18] C.T. Kwok, H.C. Man, F.T. Cheng, K.H. Lo, Developments in laser-based surface engineering processes: with particular reference to protection against cavitation erosion, Surf. Coatings Technol. 291 (2016) 189–204, https://doi.org/10.1016/j.surfcoat.2016.02.019.
[19] S.V. Kirner, T. Wirth, H. Sturm, J. Krüger, J. Bonse, Nanometer-resolved chemical analyses of femtosecond laser-induced periodic surface structures on titanium, J. Appl. Phys. 122 (2017) 104901, , https://doi.org/10.1063/1.4993128.
[20] P. Gregorčič, B. Šetina-Batič, M. Hočevar, Controlling the stainless steel surface wettability by nanosecond direct laser texturing at high fluences, Appl. Phys. A 123 (2017) 766, https://doi.org/10.1007/s00339-017-1392-5.
[21] L.B. Boinovich, A.M. Emelyanenko, A.D. Modestov, A.G. Domantovsky, K.A. Emelyanenko, Synergistic effect of superhydrophobicity and oxidized layers on corrosion resistance of aluminum alloy surface textured by nanosecond laser treatment, ACS Appl. Mater. Interfaces 7 (2015) 19500–19508, https://doi.org/10.1021/acsami.5b06217.
[22] A.-M. Kietzig, S.G. Hatzikiriakos, P. Englezos, Patterned superhydrophobic metallic surfaces, Langmuir 25 (2009) 4821–4827, https://doi.org/10.1021/la8037582.
[23] D.V. Ta, A. Dunn, T.J. Wasley, R.W. Kay, J. Stringer, P.J. Smith, C. Connaughton, J.D. Shephard, Nanosecond laser textured superhydrophobic metallic surfaces and their chemical sensing applications, Appl. Surf. Sci. 357 (2015) 248–254, https://doi.org/10.1016/j.apsusc.2015.09.027.
[24] U. Trdan, M. Hočevar, P. Gregorčič, Transition from superhydrophilic to superhydrophobic state of laser textured stainless steel surface and its effect on corrosion resistance, Corros. Sci. 123 (2017) 21–26, https://doi.org/10.1016/j.corsci.2017.04.005.
[25] R.N. Wenzel, Resistance of solid surfaces to wetting by water, Ind. Eng. Chem. 28 (1936) 988–994, https://doi.org/10.1021/ie50320a024.
[26] A.-M. Kietzig, M. Negar Mirvakili, S. Kamal, P. Englezos, S.G. Hatzikiriakos, Laser-patterned super-hydrophobic pure metallic substrates: Cassie to Wenzel wetting transitions, J. Adhes. Sci. Technol. 25 (2011) 2789–2809, https://doi.org/10.1163/016942410X549988.
[27] V.D. Ta, A. Dunn, T.J. Wasley, J. Li, R.W. Kay, J. Stringer, P.J. Smith, E. Esenturk, C. Connaughton, J.D. Shephard, Laser textured superhydrophobic surfaces and their applications for homogeneous spot deposition, Appl. Surf. Sci. 365 (2016) 153–159, https://doi.org/10.1016/J.APSUSC.2016.01.019.
[28] V. Belova, D.A. Gorin, D.G. Shchukin, H. Möhwald, Controlled effect of ultrasonic cavitation on hydrophobic/hydrophilic surfaces, ACS Appl. Mater. Interfaces 3 (2011) 417–425, https://doi.org/10.1021/am101006x.
[29] V. Belova-Magri, A. Brotchie, C. Cairós, R. Mettin, H. Möhwald, Micropatterning for the control of surface cavitation: visualization through high-speed imaging, ACS Appl. Mater. Interfaces 7 (2015) 4100–4108, https://doi.org/10.1021/am508062h.
[30] J. Gabzdyl, Fibre lasers make their mark, Nat. Photonics 2 (2008) 21–23, https://doi.org/10.1038/nphoton.2007.268.
[31] P. Gregorčič, M. Zupančič, I. Golobič, Scalable surface microstructuring by a fiber laser for controlled nucleate boiling performance of high- and low-surface-tension fluids, Sci. Rep. 8 (2018) 7461, https://doi.org/10.1038/s41598-018-25843-5.
[32] E. Pozsgai, I. Galambos, G. Dóka, L. Csóka, Use of hydrodynamic cavitation with additional high purity water for thermal water treatment, Chem. Eng. Process. - Process Intensif. 128 (2018) 77–79, https://doi.org/10.1016/J.CEP.2018.04.016.
[33] R. Terán Hilares, J.G. dos Santos, N.B. Shiguematsu, M.A. Ahmed, S.S. da Silva, J.C. Santos, Low-pressure homogenization of tomato juice using hydrodynamic cavitation technology: effects on physical properties and stability of bioactive compounds, Ultrason. Sonochem. (2019), https://doi.org/10.1016/J.ULTSONCH.2019.01.039.
[34] K. Li, M.W. Woo, H. Patel, L. Metzger, C. Selomulya, Improvement of rheological and functional properties of milk protein concentrate by hydrodynamic cavitation, J. Food Eng. 221 (2018) 106–113, https://doi.org/10.1016/J.JFOODENG.2017.10.005.
[35] S. Parthasarathy, T. Siah Ying, S. Manickam, Generation and Optimization of Palm

Oil-Based Oil-in-Water (O/W) Submicron-Emulsions and Encapsulation of Curcumin Using a Liquid Whistle Hydrodynamic Cavitation Reactor (LWHCR), (2013). DOI:10.1021/ie4008858.
[36] E. Colombo, F. Cavalieri, M. Ashokkumar, Role of Counterions in Controlling the Properties of Ultrasonically Generated Chitosan-Stabilized Oil-in-Water Emulsions, (2015). DOI:10.1021/acsami.5b02773.
[37] M. Petkovšek, M. Hočevar, P. Gregorčič, Cavitation dynamics on laser-textured surfaces, in: 10th Int. Symp. Cavitation - CAV2018, ASME, Baltimore, Maryland; USA, 2018: pp. 202–205. http://www.asme.org/about-asme/terms-of-use (accessed August 20, 2019).
[38] M. Conradi, A. Drnovšek, P. Gregorčič, Wettability and friction control of a stainless steel surface by combining nanosecond laser texturing and adsorption of superhydrophobic nanosilica particles, Sci. Rep. 8 (2018) 7457, https://doi.org/10.1038/s41598-018-25850-6.
[39] M. Dular, B. Bachert, B. Stoffel, B. Širok, Relationship between cavitation structures and cavitation damage, Wear 257 (2004) 1176–1184, https://doi.org/10.1016/j.wear.2004.08.004.
[40] P. Gregorčič, M. Conradi, L. Hribar, M. Hočevar, P. Gregorčič, M. Conradi, L. Hribar, M. Hočevar, Long-term influence of laser-processing parameters on (Super)hydrophobicity development and stability of stainless-steel surfaces, Materials (Basel) 11 (2018) 2240, https://doi.org/10.3390/ma11112240.
[41] J. Long, M. Zhong, P. Fan, D. Gong, H. Zhang, Wettability conversion of ultrafast laser structured copper surface, J. Laser Appl. 27 (2015) S29107, https://doi.org/10.2351/1.4906477.
[42] Z. Yang, X. Liu, Y. Tian, Insights into the wettability transition of nanosecond laser ablated surface under ambient air exposure, J. Colloid Interface Sci. 533 (2019) 268–277, https://doi.org/10.1016/j.jcis.2018.08.082.
[43] P Gregorčič, Comment on “Bioinspired Reversible Switch between Underwater Superoleophobicity/Superaerophobicity and Oleophilicity/Aerophilicity and Improved Antireflective Property on the Nanosecond Laser-Ablated Superhydrophobic Titanium Surfaces”, ACS Appl. Mater. Interfaces (2020), https://doi.org/10.1021/acsami.9b23462.

Supporting Information

Surface functionalization by nanosecond-laser texturing for controlling hydrodynamic cavitation dynamics

Martin Petkovšek[a,*], Matej Hočevar[b], Peter Gregorčič[a]

[a]*Faculty of Mechanical Engineering, University of Ljubljana, Aškerčeva 6, 1000 Ljubljana, Slovenia*

[b]*Institute of Metals and Technology, Lepi pot 11, 1000 Ljubljana, Slovenia*

Corresponding author:

** E-mail: martin.petkovsek@fs.uni-lj.si (M. Petkovšek)*

Table of Contents

1 Texturing of stainless steel cylinders by laser pulses

The stainless steel cylinders were mounted on the rotational stage with an angular resolution of 0.005° in a way that their symmetrical axis was aligned with the stage axis of the rotation. The top part of the cylinder surface was placed into the focus of an F-theta lens with a focal length of f_L = 163 mm. The beam diameter on the lens equaled D = 7.5 mm, while the beam quality was M^2 = 1.3. Thus, the beam waist radius w_0 for the wavelength of our laser source (λ = 1060 nm) can be estimated as:

$$w_0 = \frac{2M^2 \lambda f_L}{\pi D} = 19\ \mu\text{m} \qquad \text{(S1)}$$

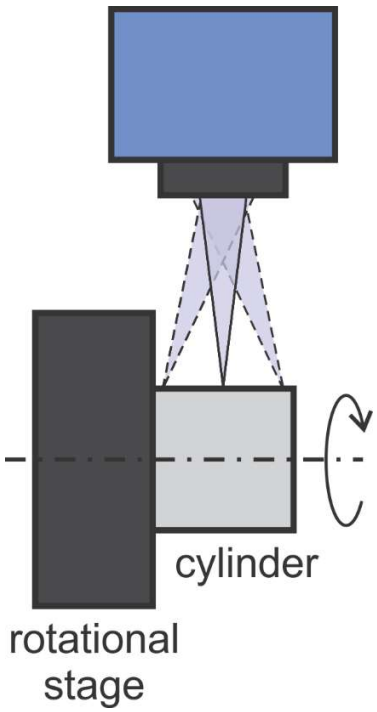

Figure S1. Presentation of the laser system for texturing cylinders.

2 Laser processing parameters

The processing parameters that were used to texture the surfaces of the cylinders (the pulse duration t_{FWHM}, pulse frequency f_p, average power P, scanning velocity v, scanning line separation Δy, and number of passes over the same line N) are presented in Table S1. Additionally, the pulse energy E_p was calculated as a ratio between the average power P and the pulse frequency f_p

$$E_p = \frac{P}{f_p} \tag{S2}$$

and the pulse fluence F_p was calculated as pulse energy E_p per area within a beam waist radius w_0

$$F_p = \frac{E_p}{\pi w_0^2}. \tag{S3}$$

The pulse separation Δx can be obtained as a ratio between the scanning velocity v and the pulse frequency f_p

$$\Delta x = \frac{v}{f_p}, \tag{S4}$$

while the pulse overlapping δ equals to:

$$\delta = 1 - \frac{\Delta x}{2w_0}. \tag{S5}$$

The energy per length is calculated as

$$E / L = N \frac{P}{v}. \tag{S6}$$

In case of drilling, the total energy per spot is calculated instead the energy per length.

Table S1. Laser processing parameters.

Sample	t_{FWHM} [ns]	f_p [kHz]	P [W]	v [mm/s]	Δy [μm]	N	E_p [μJ]	F_p [J cm^{-2}]	δ	Energy per length
Dimpled (S2)	10	900	19	/	/	27000 per spot	21	1.9	100%	0.57 J per spot
Velvet (S3)	28	90	19	540	11	1	211	18.6	84%	0.35 J cm^{-1}
Oxidized (S4)	10	100	3.7	300	0.9	1	37	3.3	92%	0.12 J cm^{-1}
Waved (S5)	28	90	19	540	67	1	211	18.6	84%	0.35 J cm^{-1}
Grooved (S6)	28	90	19	540	130	10	211	18.6	84%	3.5 J cm^{-1}

3 SEM images of the laser-textured surfaces

SEM images of surfaces are shown in Figures S2 – S10. Images were recorded using a JEOL JSM-6500F scanning electron microscope, in some of them the electron beam was tilted by ~65° regarding the surface normal.

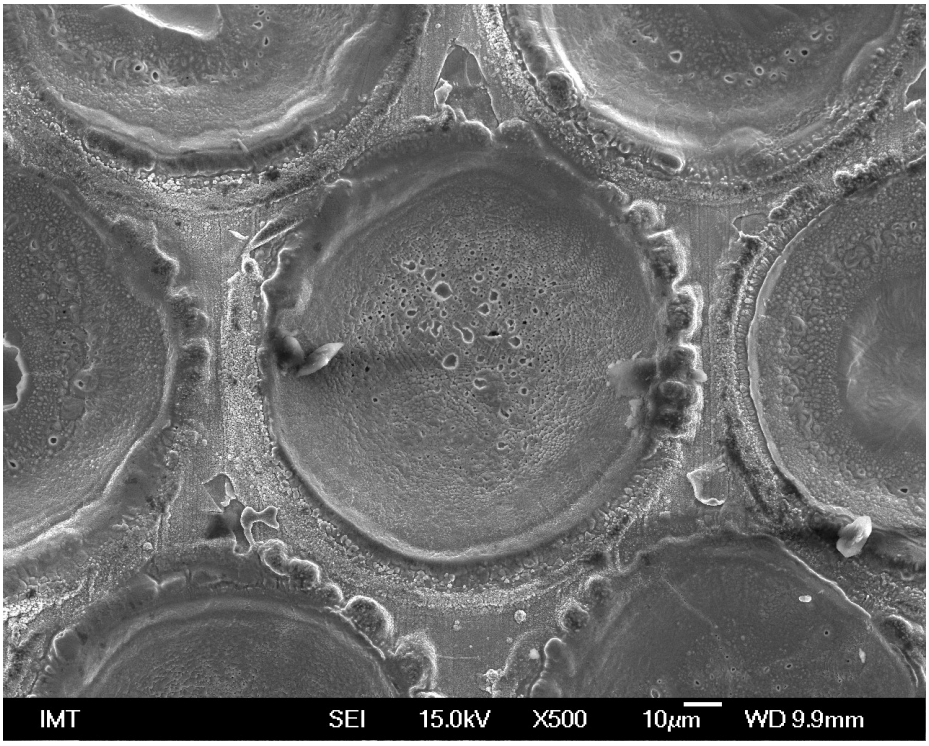

Figure S2. SEM image of the laser-textured dimpled surface (S2).

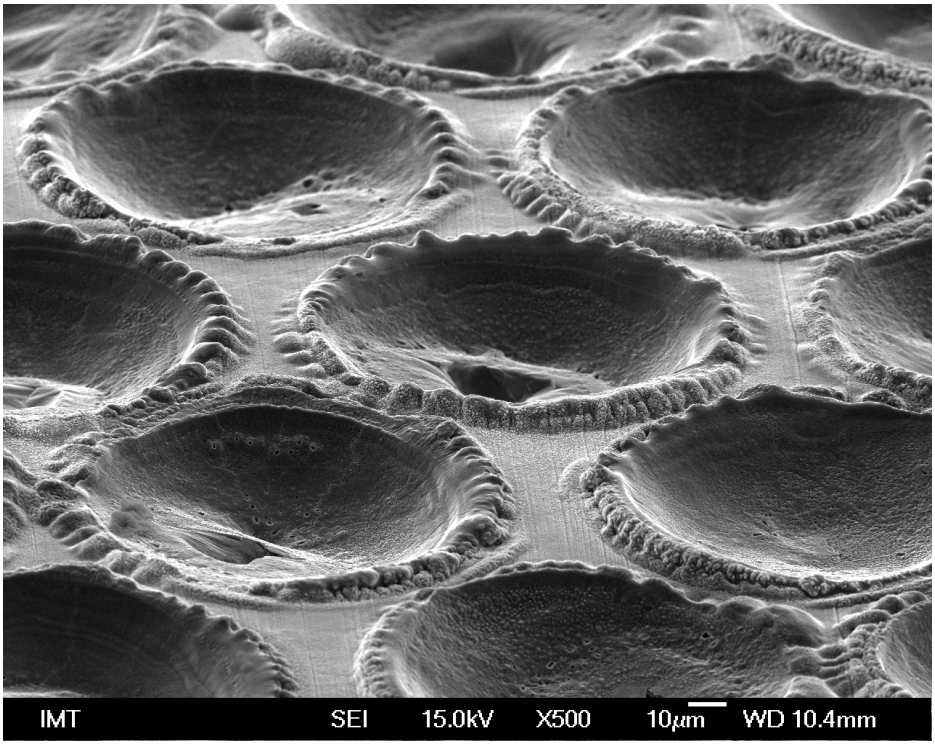

Figure S3. SEM image of the laser-textured dimpled surface (S2) in a tilted mode.

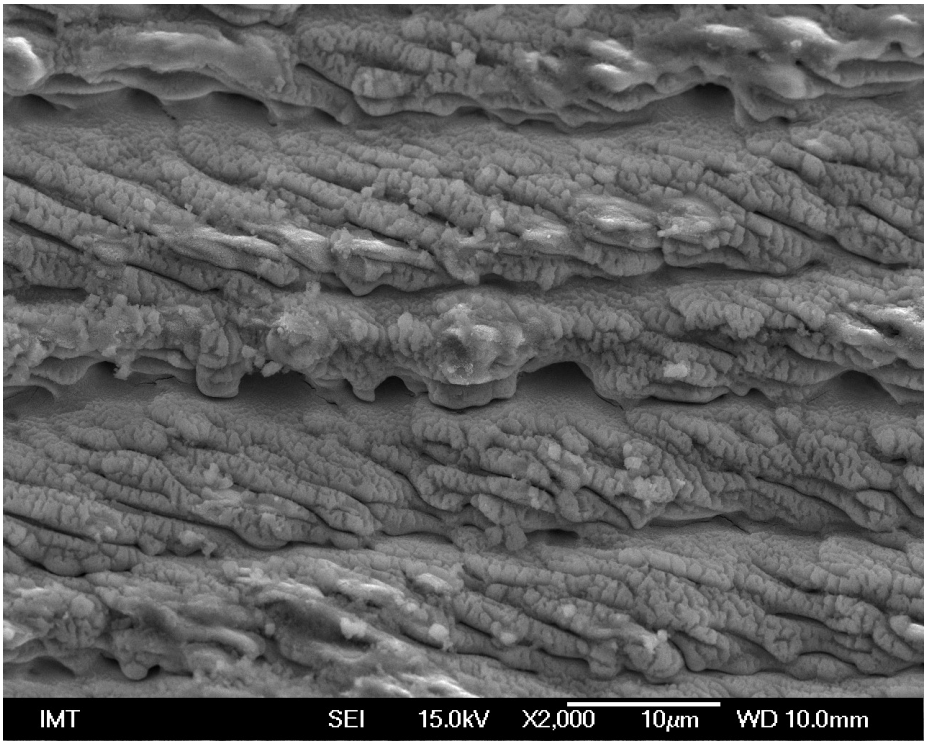

Figure S4. SEM image of the laser-textured velvet surface (S3).

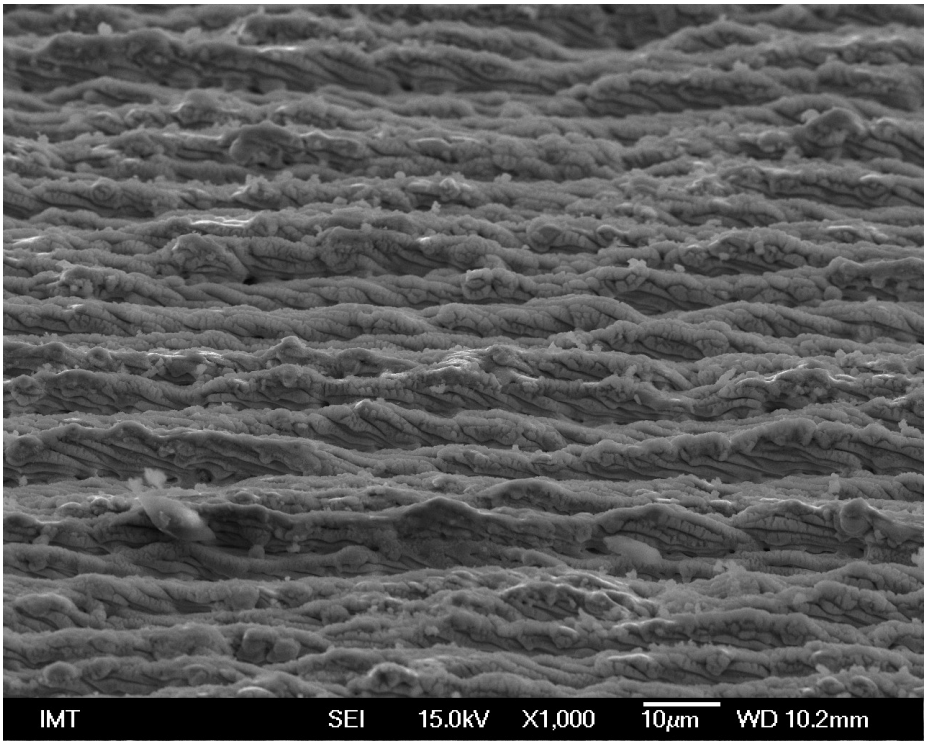

Figure S5. SEM image of the laser-textured velvet surface (S3) in a tilted mode.

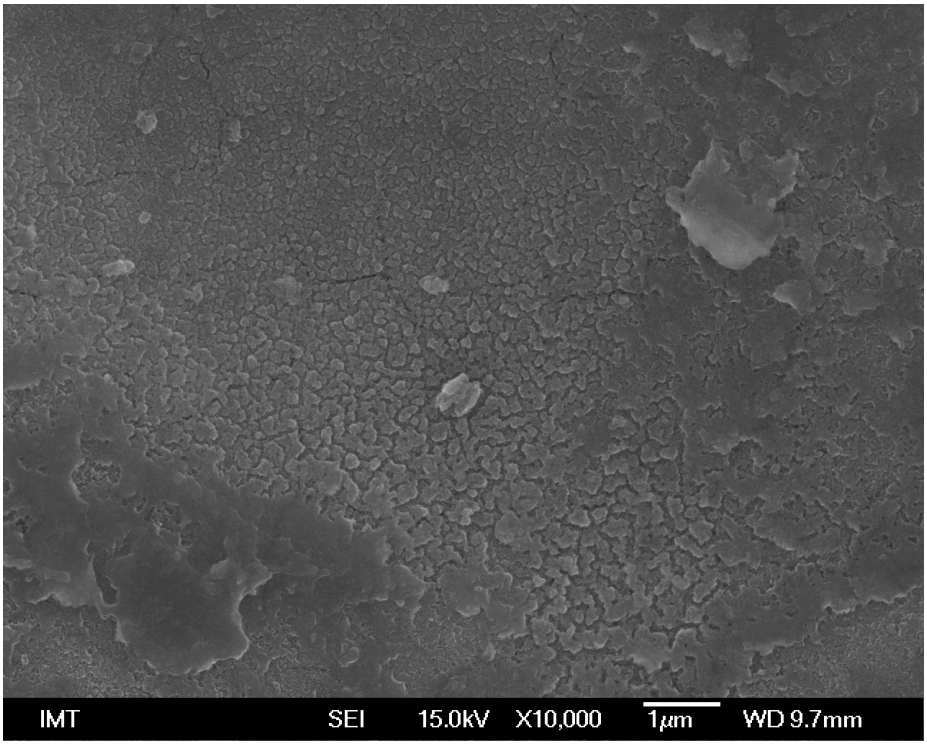

Figure S6. SEM image of the laser-textured oxidized surface (S4).

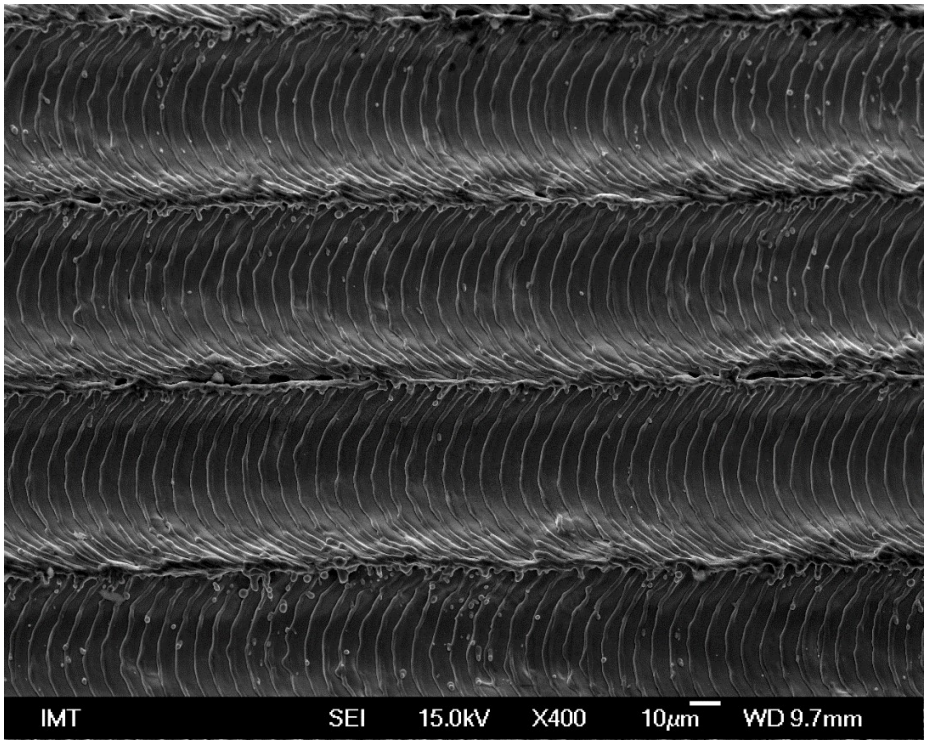

Figure S7. SEM image of the laser-textured waved surface (S5).

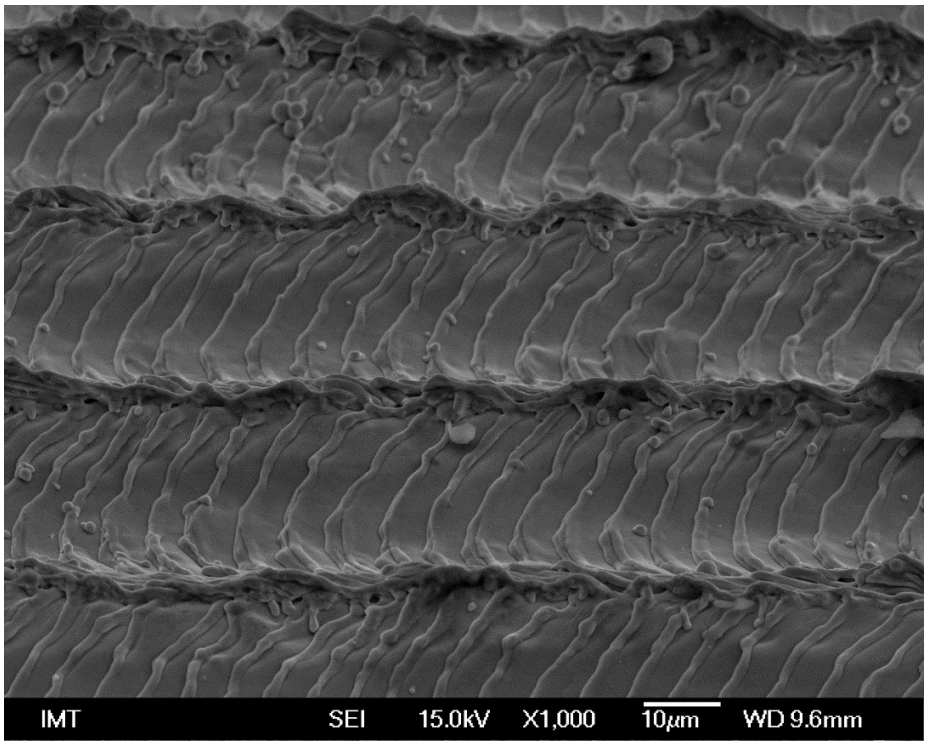

Figure S8. SEM image of the laser-textured waved surface (S5) in a tilted mode.

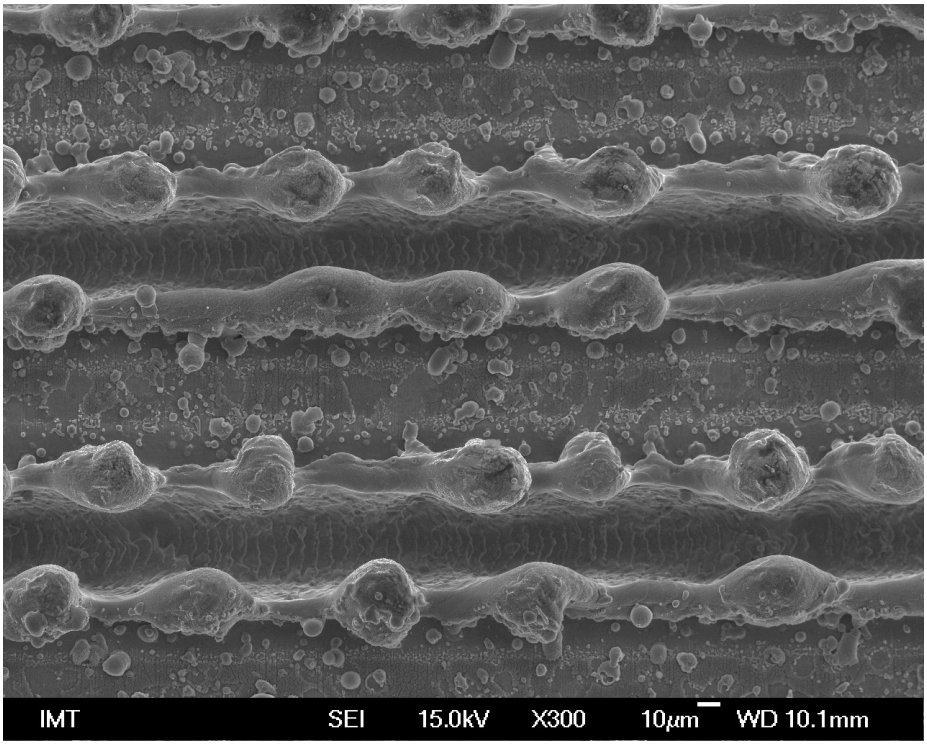

Figure S9. SEM image of the laser-textured grooved surface (S6).

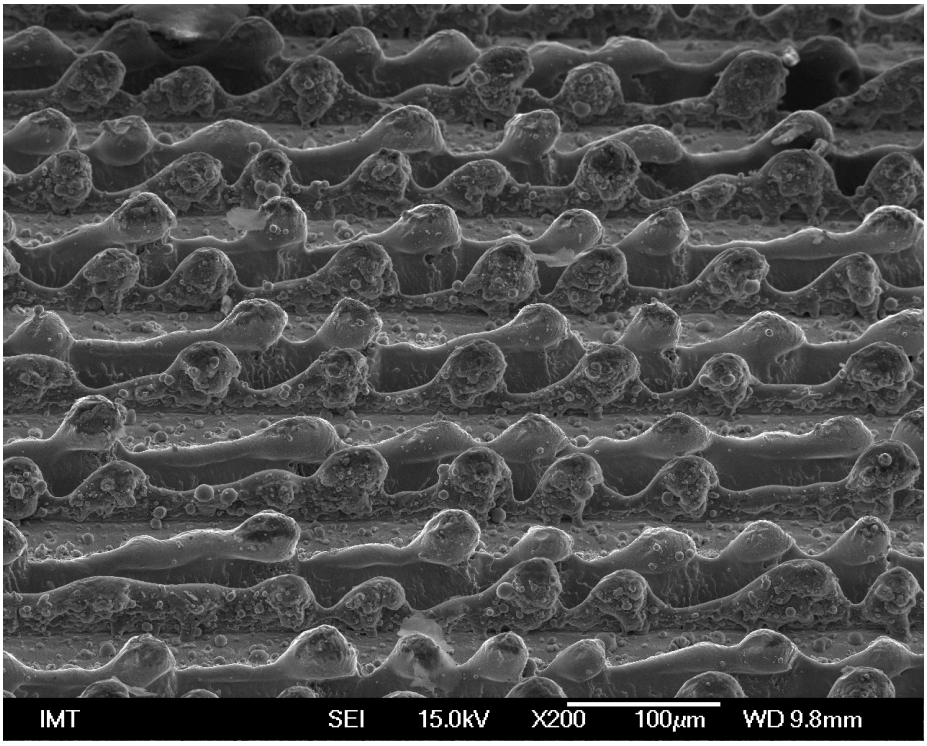

Figure S10. SEM image of the laser-textured grooved surface (S6) in a tilted mode.

4 Surface parameters

The average height of the selected area (S_a parameter)

Optical 3D metrology system, model Alicona Infinite Focus (Alicona Imaging GmbH), and IF-MeasureSuite (Version 5.1) were used to evaluate the average height of the selected area S_a parameter, defined as:

$$S_a = \frac{1}{L_x}\frac{1}{L_y}\int_0^{L_y}\int_0^{L_x}|z(x,y)|\,dxdy, \tag{S7}$$

where L_x and L_y stand for the acquisition lengths of the selected surface in the x and y directions, respectively and $|z(x,y)|$ is the absolute value of the height.

The roughness of a profile (R_a parameter)

To enable better comparison with other (existing and future) similar studies, the roughness of a profile R_a was also evaluated, although in some samples, like reference (S1), dimpled (S2), and oxidized (S4) it is not a good measure of roughness. The R_a is defined as:

$$R_a = \frac{1}{L_x}\int_0^{L_x}|z(x)|\,dx, \tag{S8}$$

were L_x stands for the acquisition length and $|z(x)|$ is the absolute value of the height. The parameter R_a was measured in the following way:

- for the reference sample (S1) it was measured parallel to the cylinder axis (since this sample was polished during the rotation and the abrasion occurs in the direction, perpendicular to the cylinder axis;
- for the dimpled sample (S2) it was measured across the centers of the laser-drilled holes;
- for the oxidized sample (S4) it was measured along the cylinder axis ***and*** in the perpendicular direction;
- for other samples [velvet (S3); waved (S5); and grooved (S6)] it was measured perpendicular to the laser scanning lines.

In all cases, the R_a parameter was measured on the length of L_x > 14 mm. Since enough long L_X was used, the measured R_a parameter is very similar to the S_a parameter.

The peak-to-peak amplitudes

Profile curves of all the tested samples are revealed on Figures S11-S16. In the case of the dimpled (S2) surface, the profile curve is measured along the centers of the holes, while in the case of the velvet (S3), waved (S5) and grooved (S6) surfaces, the profile curve is measured perpendicular to the laser scanning lines. The presented results reveal that reference (S1) and oxidized (S4) surfaces do not express any periodicity in the profile curve, while the periodicity of the profile curve decreases by decreasing the scanning line separation [e.g., for the velvet surface (S3)].

The peak-to-peak amplitude was measured as schematically shown in Figure S12. It presents an average height between the valley and the peak marked by the circles (for the valleys) and the squares (for the peaks) of the same color in Figure S12.

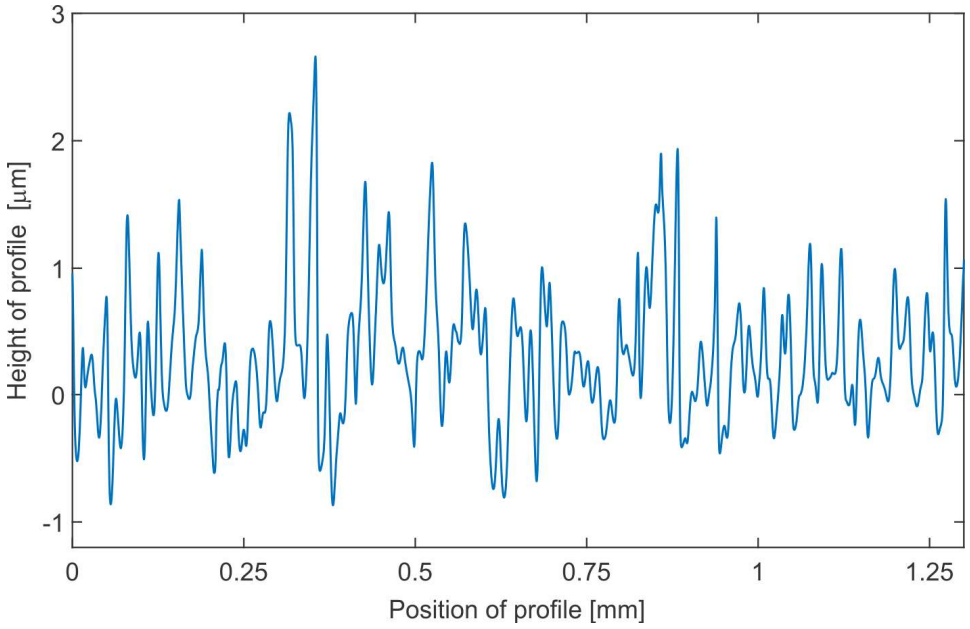

Figure S11. Profile curve of the polished (S1), reference surface.

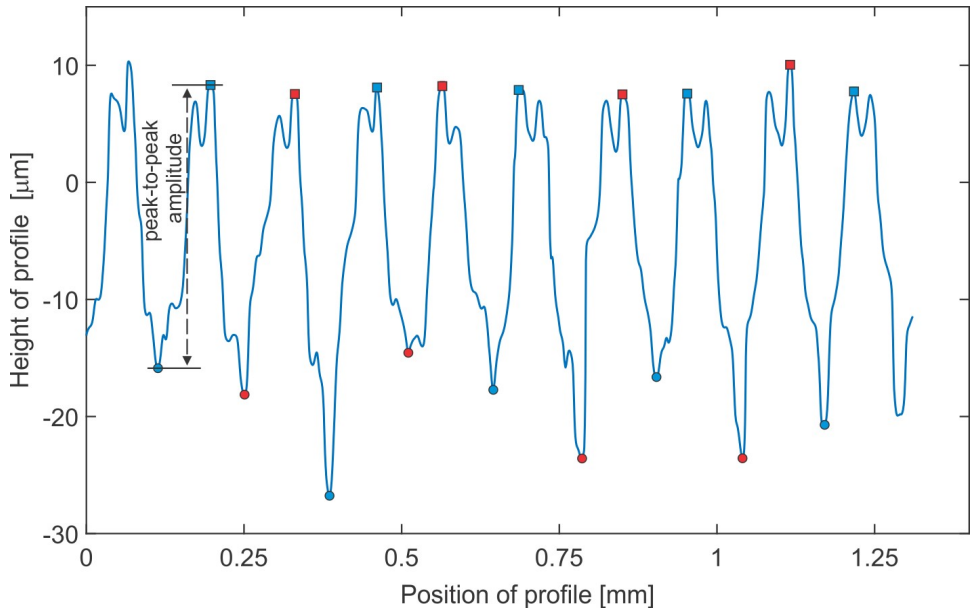

Figure S12. Profile curve of the dimpled (S2) surface. The peak-to-peak amplitude is also presented.

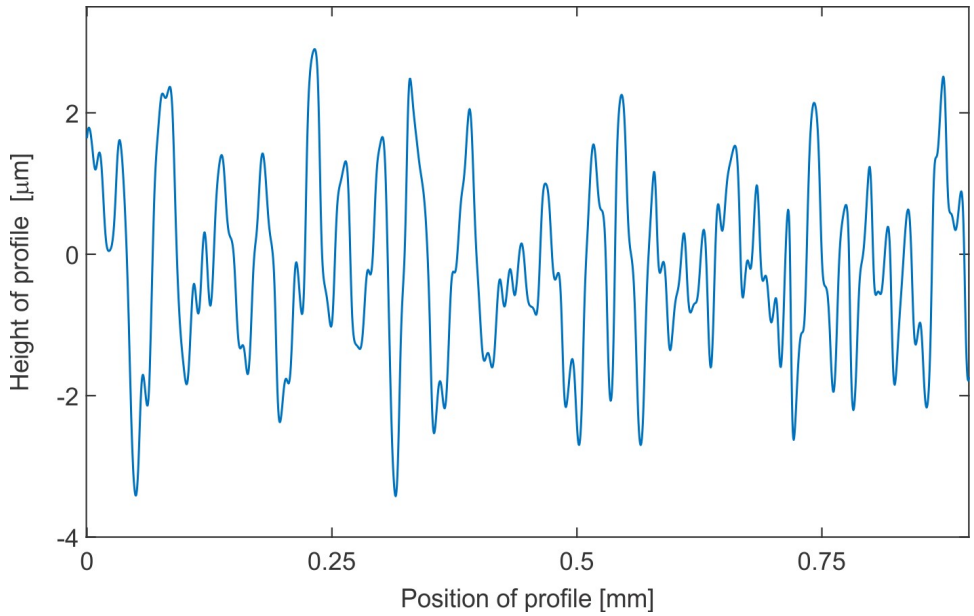

Figure S13. Profile curve of the velvet (S3) surface.

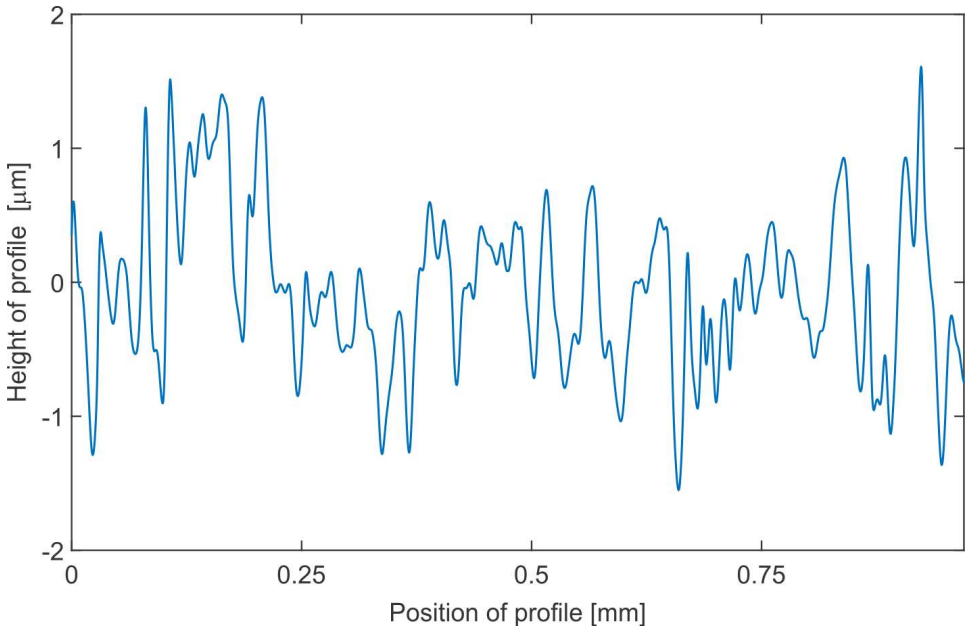

Figure S14. Profile curve of the oxidized (S4) surface.

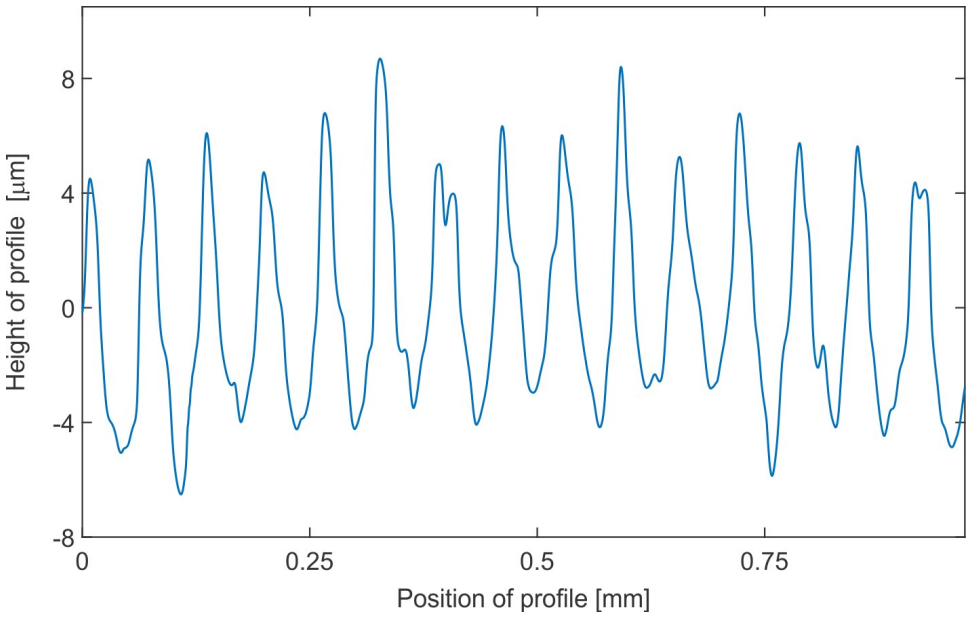

Figure S15. Profile curve of the waved (S5) surface.

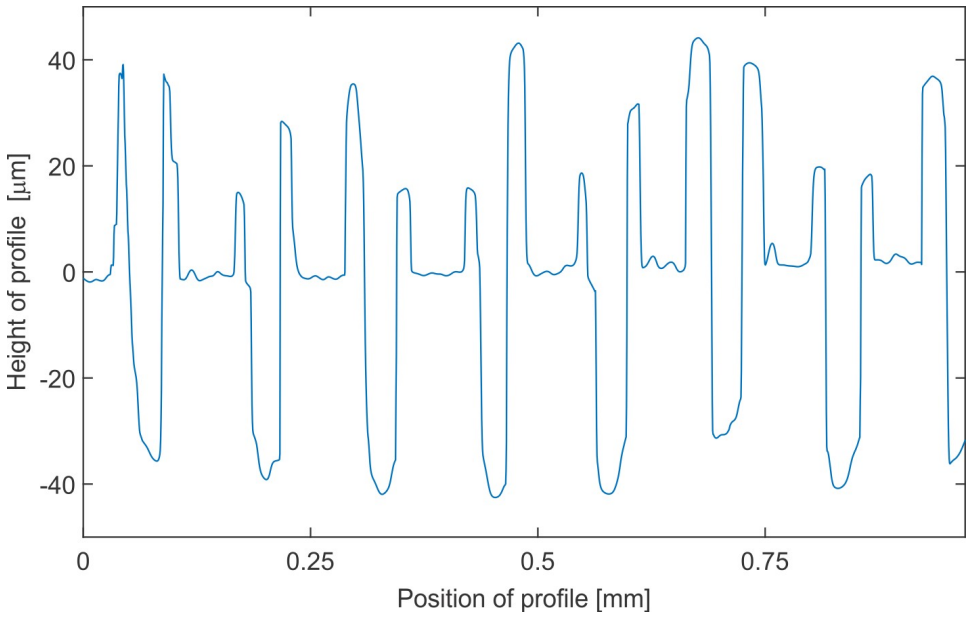

Figure S16. Profile curve of the grooved (S6) surface.

5 High-speed visualization of cavitation behind the specimens

Image time sequences of cavitation behind various specimens are presented on Figures S17-S21. The time step between two images equals 0.5 ms. Red circles present specimen position and the fluid flow is from right to left.

On Figure S17 at $\sigma = 2.3$, almost no cavitation can be noticed, since this operating point was chosen at the point of cavitation incipient on a reference, i.e., highly polished specimen.

On Figure S18 at $\sigma = 1.8$ the initial cavitation can be seen on the grooved, waved, oxidized, polished and velvet specimens, but no cavitation can be noticed on the dimpled specimen.

Developed cavitation behind all the specimens at $\sigma = 1.4$ can is observed on Figure S19, where the dimpled, velvet and oxidized sample do not form typical von Karman cavitation shape, as it can be seen on the polished, waved and grooved specimens.

On Figure S20 at $\sigma = 1.2$ fully developed cavitation is visible behind all the specimens, but one can distinct different dynamic nature of cavitation behavior between various specimens. Once again, cavitation behind the dimpled and the velvet specimens does not form a distinct von Karman shape as it can be seen, e.g., behind the polished specimen. The polished, oxidized, waved and grooved specimens also form strong cavitation shedding, which is in case of the dimpled and the velvet specimen diminished.

On Figure S21 at $\sigma = 1.0$ cavitation is on the boundary between fully developed and supercavitation. At this cavitation number, distinct differences are visible between cavitation dynamics behind various specimens. While cavitation behind the polished specimen still preserves von Karman dynamic behavior, cavitation behind the dimpled specimen acts much less dynamic and more stable without shedding.

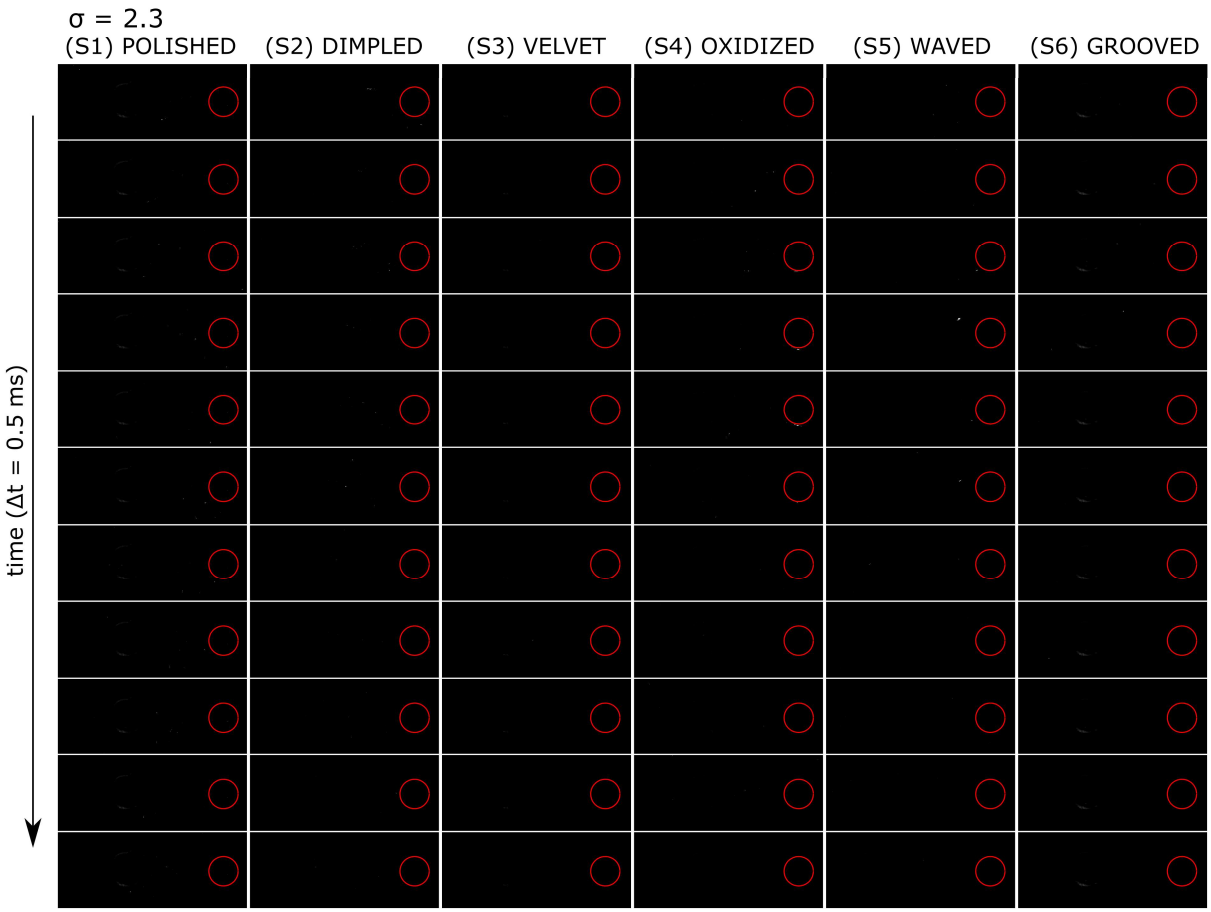

Figure S17. Visualization images of cavitation behind the specimens at σ = 2.3. Time step between two images equals 0.5 ms.

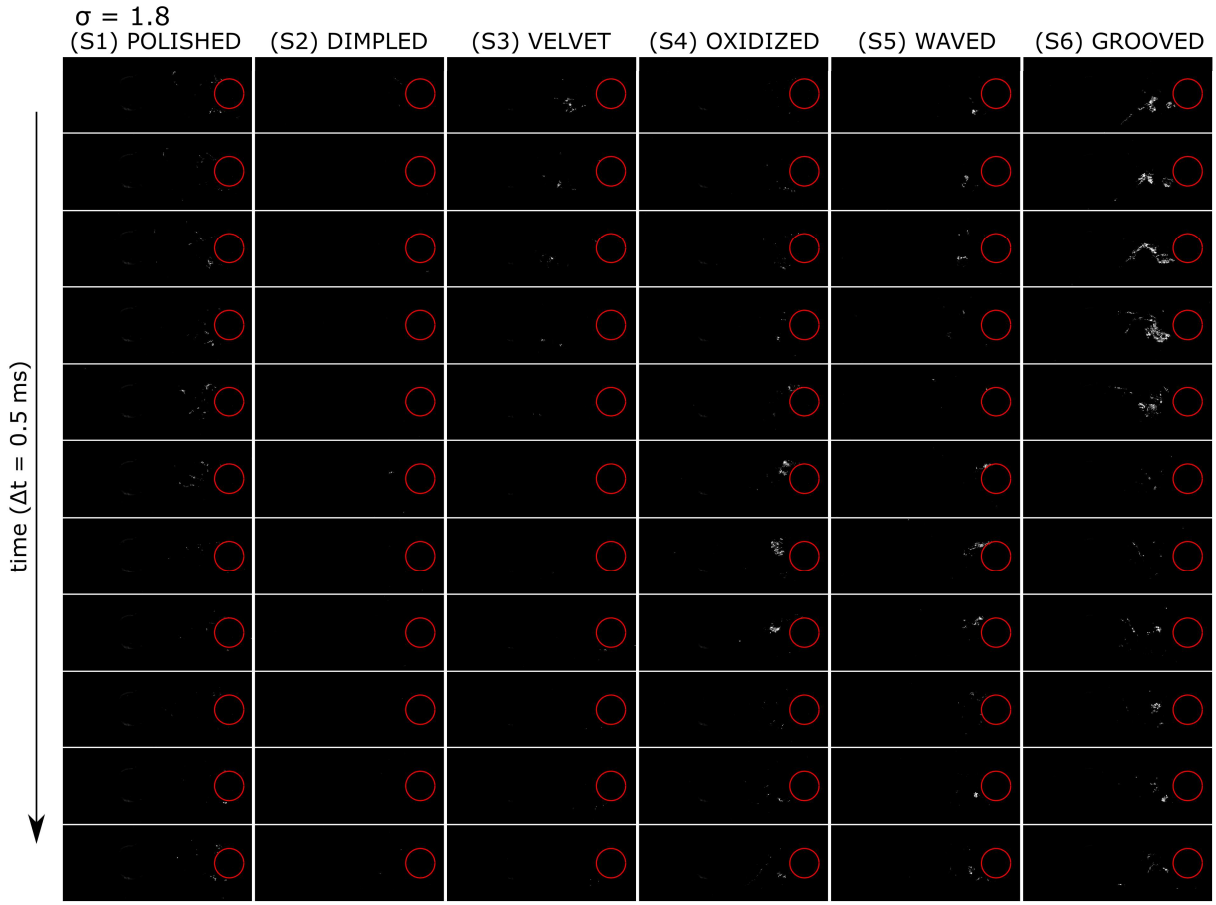

Figure S18. Visualization images of cavitation behind the specimens at σ = 1.8. Time step between two images equals 0.5 ms.

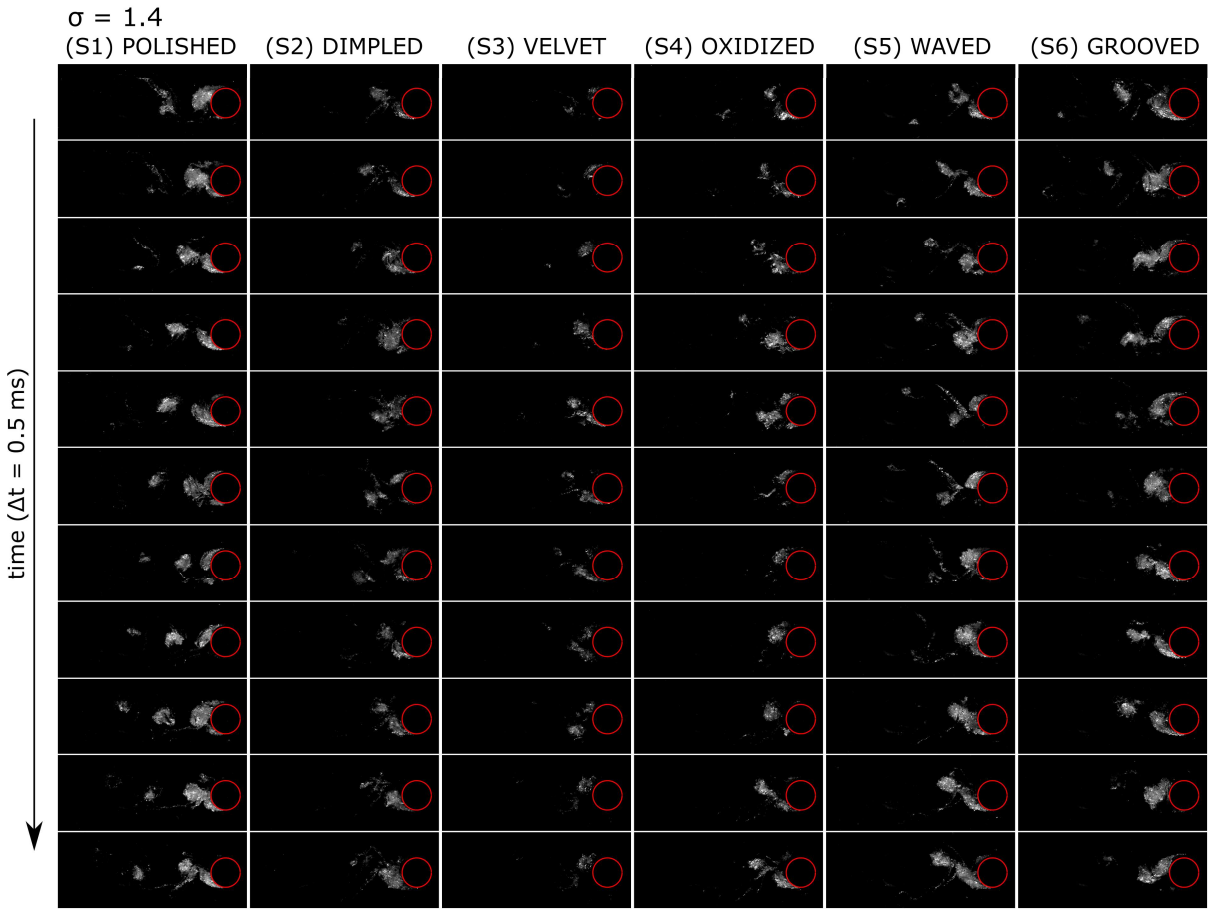

Figure S19. Visualization images of cavitation behind the specimens at σ = 1.4. Time step between two images equals 0.5 ms.

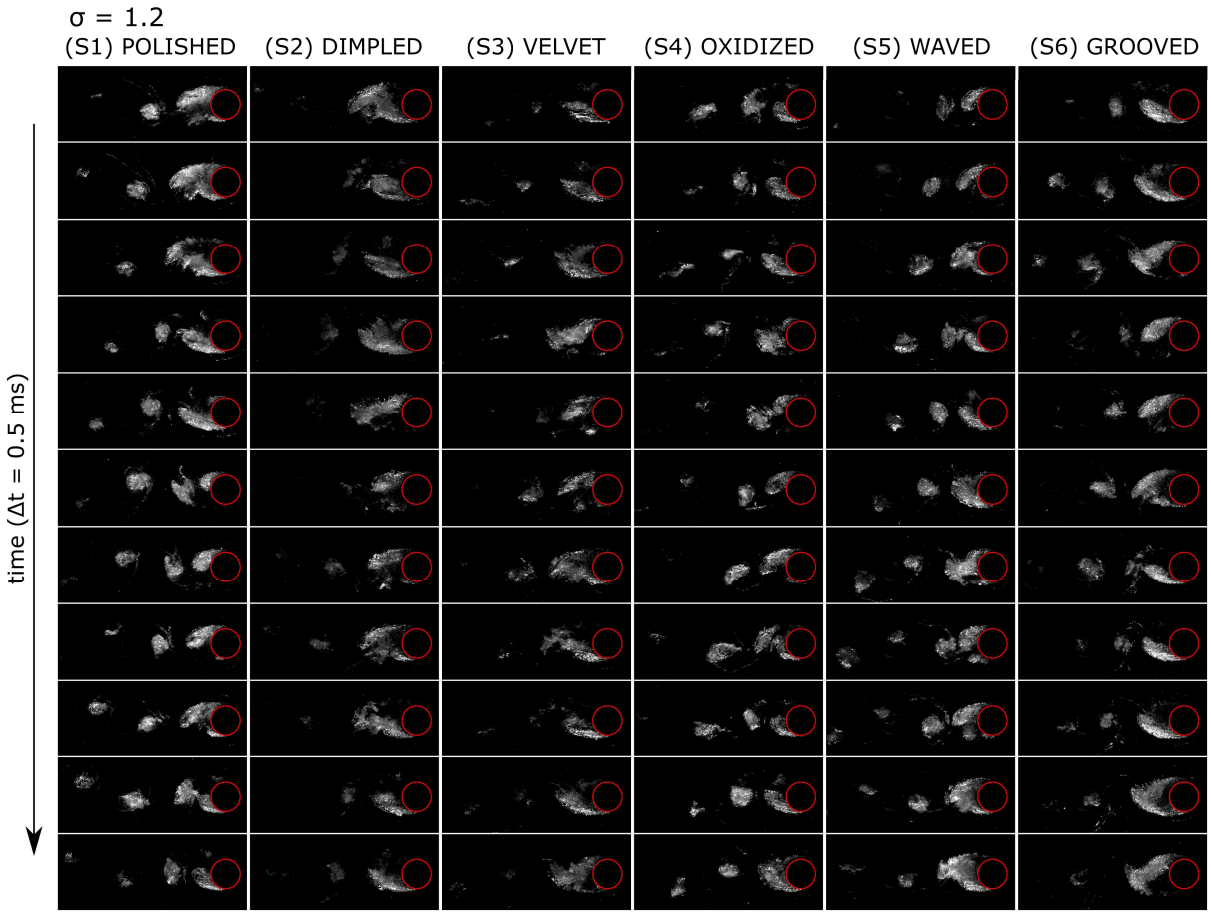

Figure S20. Visualization images of cavitation behind the specimens at σ = 1.2. Time step between two images equals 0.5 ms.

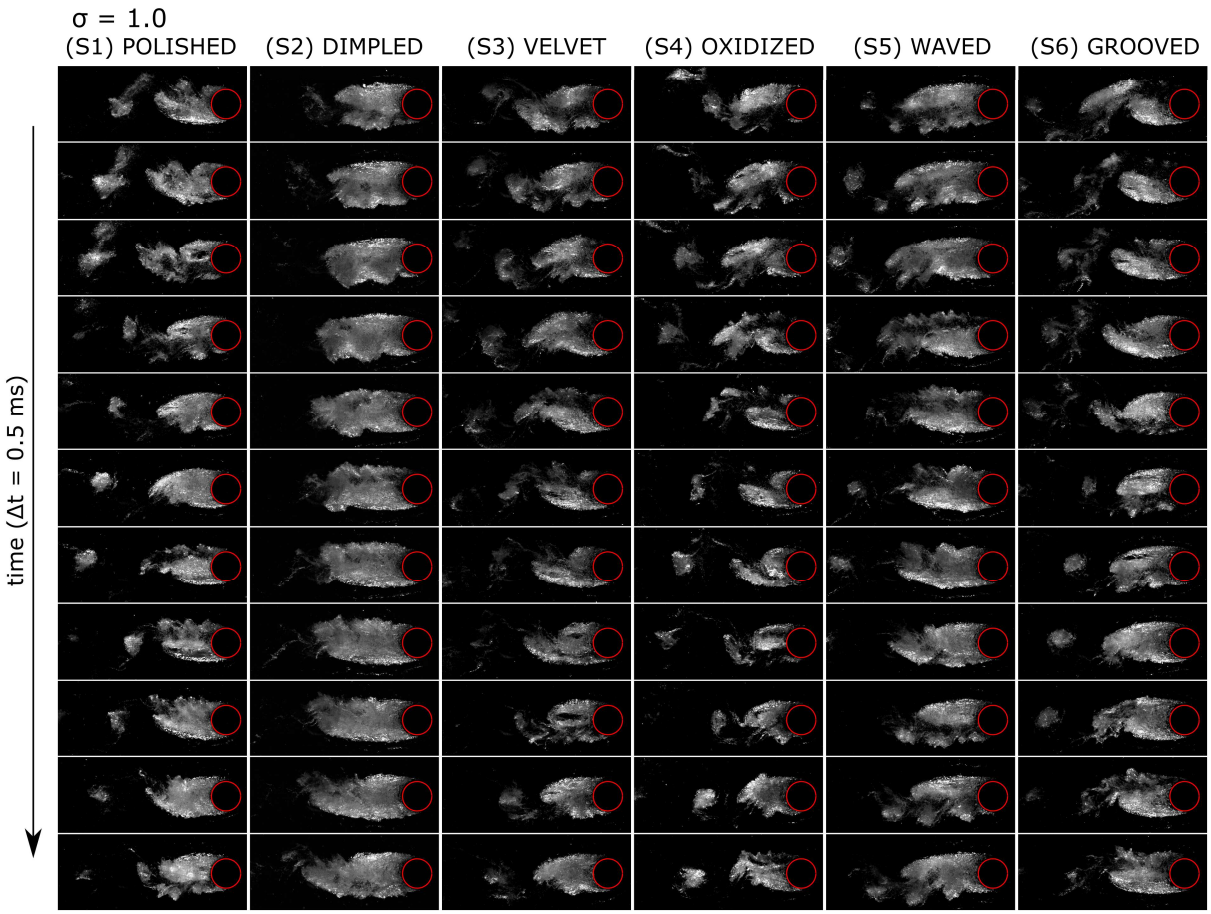

Figure S21. Visualization images of cavitation behind the specimens at σ =1.0. Time step between two images equals 0.5 ms.

6 Determination of the cavitation length

The heights of the acquired images (an example is shown on the bottom of Figure S22) equal H = 256 px, while their widths equal W = 640 px. Thus, each (i-th) acquired image can be presented as the following matrix:

$$I_i(m,n) = \begin{bmatrix} (1,1) & \cdots & (1,W) \\ \vdots & \ddots & \vdots \\ (H,1) & \cdots & (H,W) \end{bmatrix}. \tag{S9}$$

In Equation (S9), each pixel at (m,n) position can take an integer value between 0 and 255, since 8-bit monochrome images were used for the image processing.

For the each tested sample at the each flow rate, we acquired N = 10,000 frames. We have divided the whole image sequence onto 25 sequences, each containing N_p = 400 frames. This allowed us to calculate the average length (as an arithmetic mean) as well as the length variations (as a standard deviation).

Partial sequence of N_p = 400 frames was chosen according to the main distinct shedding frequency of the cavitation, which in our case equals approximately 500 Hz. For the visualization we used framerate of 20,000 fps. To process approximately 10 cycles of the cavitation shedding within a single partial sequence, this partial sequence should contain N_p = 20,000/500×10 = 400 frames.

For each sequence (p = 1, …, 25), the sum value of the gray level distribution is calculated as:

$$I_{\mathrm{tot}}^{p}(m,n) = \sum_{i=1}^{N_p} I_{\mathrm{i}}(m,n) \tag{S10}$$

To determine the length of the cavitation, the sum value of the gray level distribution for a partial sequence was converted into the vector (with length of W elements), as:

$$G^{p}(m) = \sum_{n=1}^{H} I_{\mathrm{tot}}(m,n) = \left[g_1, g_2, \cdots g_W \right]. \tag{S11}$$

Each g_m element in Equation (S11) equals the sum of the values in the m-th column of the I_{tot}^{p}. The vector of the gray level distribution $G^p(m)$ was further normalized as:

$$G^{p}_{\mathrm{norm}}(m) = \frac{G^{p}(m)}{G_{\max}}. \tag{S12}$$

Here, the maximum value $G_{\max}$ was chosen as the average of maxima of $G^{p}(m)$ for the reference, polished (S1) sample at each flow rate. The maximum values used for the normalization as a function of the Reynolds numbers are shown in Figure S23. The increase of the normalization value $G_{\max}$ by the Reynolds number indicates the increase of the cavitation intensity.

As an example, all 25 normalized gray level lines $G^{p}_{\mathrm{norm}}(m)$ for the polished sample (S1) at σ = 1.4 are shown in Figure S22.

In all the images, the center of the cylinder (see the bottom of Figure S22) was positioned as m_{c} = 575 px. The position m_{L}, defined as the end of the cavitation, was determined as m, where the normalized gray level line equals $G^{p}_{\mathrm{norm}}(m_{\mathrm{L}}) = 0.5$ (these positions are marked by the circles in Figure S22). The cavitation length within each partial sequence was further calculated as:

$$L_{p} = \kappa \left| m^{p}_{\mathrm{L}} - m_{\mathrm{c}} \right|, \tag{S13}$$

where κ = 92.6 μm/px is the magnification of our optical system and was determined by appropriate calibration.

By using Equation (S13), 25 different values of L_{p} (for p = 1, …, 25) were determined for each testing parameter. From them, we have calculated the cavitation length as an arithmetic mean and corresponding standard deviation. They are listed in Table S2.

Table S2. Cavitation characteristics for tested samples at various flow conditions.

Specimen	σ (-)	*Re* (-)	*L* (mm)	*St* (-)
Polished (S1)	2.6	83,000	-	1.09 ± 0.2
	2.3	89,000	-	0.95 ± 0.1
	1.8	100,000	11.4 ± 0.9	0.74 ± 0.1
	1.4	111,000	12.3 ± 0.3	0.60 ± 0.2
	1.2	122,000	15.7 ± 0.8	0.49 ± 0.1
	1.0	133,000	24.2 ± 1.1	0.48 ± 0.1
Dimpled (S2)	2.6	83,000	-	-
	2.3	89,000	-	0.87 ± 0.2
	1.8	100,000	-	0.75 ± 0.3
	1.4	111,000	9.8 ± 0.5	0.73 ± 0.1
	1.2	122,000	14.1 ± 0.7	0.47 ± 0.4
	1.0	133,000	22.6 ± 1.6	0.96 ± 0.4
Velvet (S3)	2.6	83,000	-	-
	2.3	89,000	-	0.82 ± 0.6
	1.8	100,000	3.0 ± 0.7	0.80 ± 0.4
	1.4	111,000	7.8 ± 0.7	0.76 ± 0.2
	1.2	122,000	13.2 ± 0.7	0.49 ± 0.1
	1.0	133,000	21.0 ± 1.2	0.86 ± 0.2
Oxidized (S4)	2.6	83,000	-	-
	2.3	89,000	-	0.91 ± 0.3
	1.8	100,000	3.2 ± 1.0	0.84 ± 0.7
	1.4	111,000	10.7 ± 0.6	0.79 ± 0.2
	1.2	122,000	15.9 ± 1.0	0.48 ± 0.1
	1.0	133,000	22.9 ± 1.1	0.80 ± 0.2
Waved (S5)	2.6	83,000	-	1.02 ± 0.0
	2.3	89,000	-	0.95 ± 0.0
	1.8	100,000	-	0.88 ± 0.3
	1.4	111,000	13.0 ± 0.6	0.73 ± 0.1
	1.2	122,000	16.8 ± 0.9	0.52 ± 0.1
	1.0	133,000	25.7 ± 1.1	0.55 ± 0.2
Grooved (S6)	2.6	83,000	-	1.35 ± 0.2
	2.3	89,000	-	1.19 ± 0.2
	1.8	100,000	12.8 ± 0.8	0.93 ± 0.2
	1.4	111,000	12.5 ± 0.5	0.84 ± 0.2
	1.2	122,000	17.6 ± 0.5	0.48 ± 0.1
	1.0	133,000	32.3 ± 2.0	0.48 ± 0.1

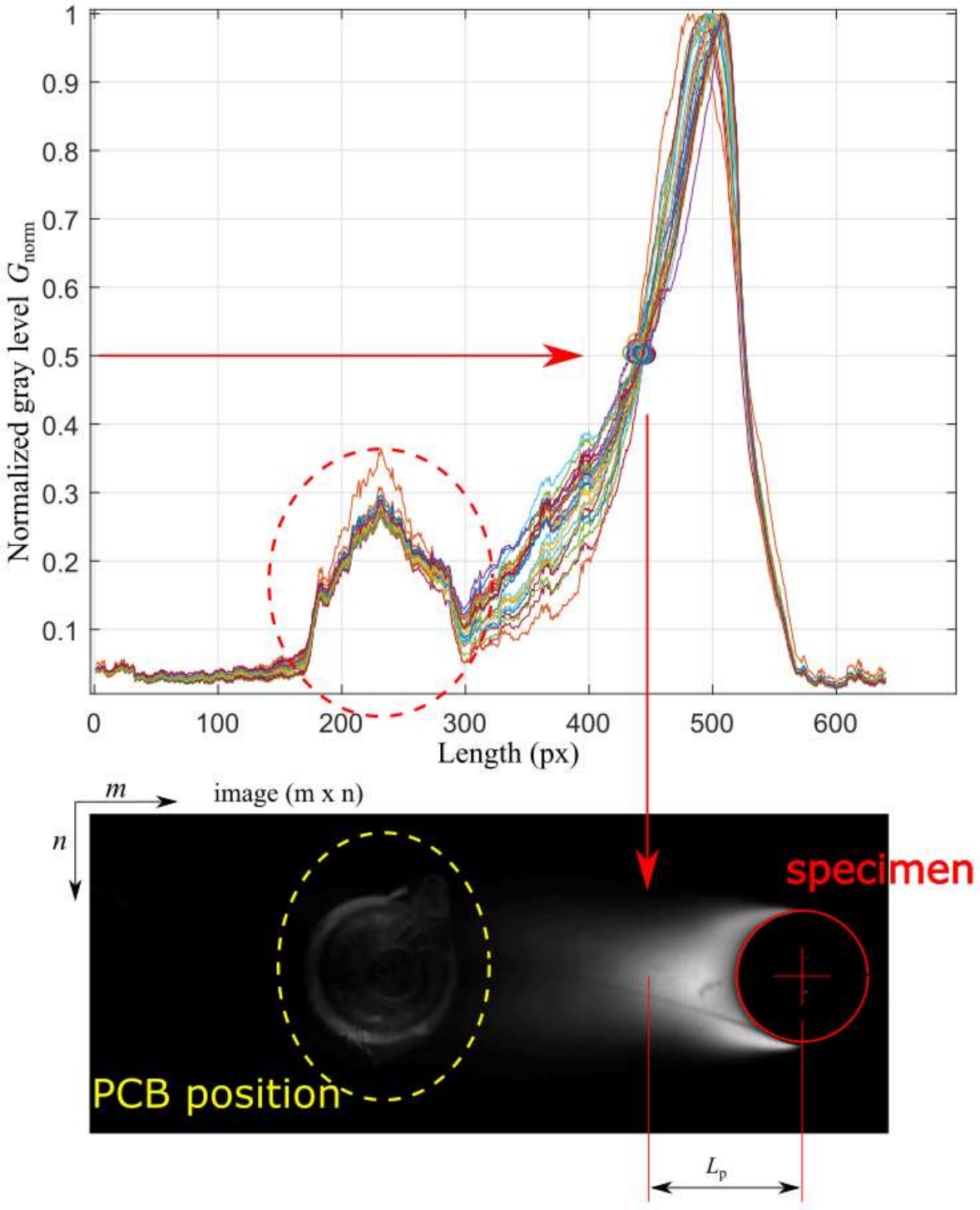

Figure S22. Determination of the cavitation length – an example for polished sample S1 at σ = 1.4.

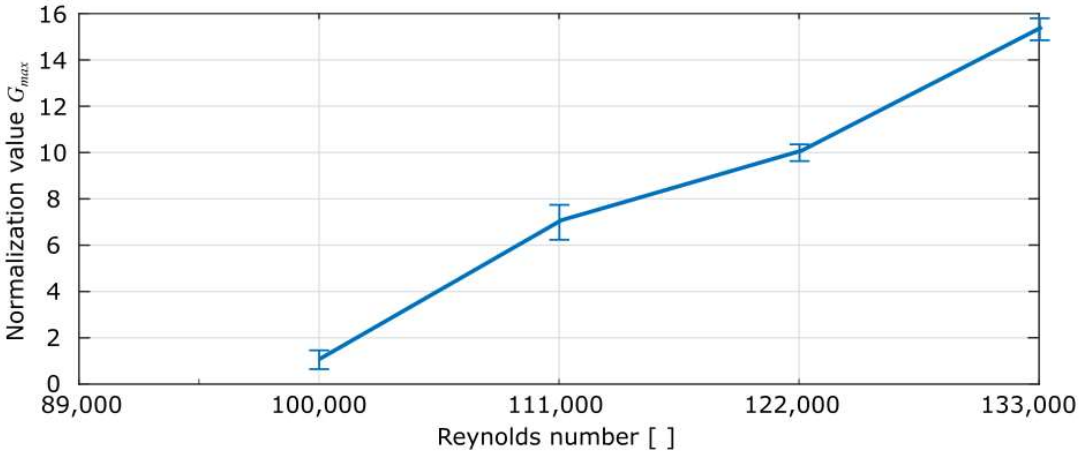

Figure S23. Normalization values $G_{\max}$ in dependence of Reynolds number.

7 Validation of the frequency response

The validation of the frequency response was performed by comparison between:

- the frequency spectra, measured by the hydrophone RESON TC4013 (the violet curve in Figure S24);
- the frequency spectra, measured by the high frequency pressure transducer PCB 113B28 (the green curve in Figure S24);
- and the frequency spectra, calculated from the high-speed visualization (the red and the blue curves in Figure S24).

Figure S24 shows an example of frequency validation for the polished specimen (S1) at cavitation number 1.2. Typical signals (i.e., pressure as a function of time), measured by the hydrophone and PCB are shown in Figure S25. From this signal, the frequency spectra (the green and the violet curves) in Figure S24 were obtained by using the Fast Fourier Transformation (FFT).

The frequency response from visualization was calculated at two different regions of interest (ROI), marked as ROI-1 and ROI-2 in images in Figure S24. At each image, all the pixel values within each ROI were summed. The sum of the ROI pixels as a function of time was further transformed into the frequency domain by FFT. In this way, the blue curve for ROI-1 and the red curve for ROI-2 were calculated.

A typical shedding frequency of the cavitation behind the selected specimen is clearly visible as a frequency peak at 530 Hz in the PCB, hydrophone and ROI-1 spectra. This peak at ROI-1 spectrum

perfectly correlates by the frequency response measured by the hydrophone and the PCB, since ROI-1 was chosen at the same position as the PCB and the hydrophone were mounted.

When the frequency response from the visualization is calculated from the ROI-2, the peak corresponding to the shedding frequency appears at $\frac{530\ \text{Hz}}{2} = 265\ \text{Hz}$. This happens, since the cavitation alternates between the upper and the bottom side of the cylinder. Thus, at ROI-2, only the half of the shedding frequency is measured.

Comparing the frequency spectra from the hydrophone and PCB, one can notice that PCB sensor amplifies frequencies (300 Hz – 350 Hz) that are approximately half of the amplified hydrophone frequencies (600 Hz – 700 Hz). Since the PCB pressure sensor is mounted 30 mm downstream from the specimen, it may sense predominately pressure oscillations caused by cavitation growth. On the other hand, the hydrophone is located 90 mm downstream. Thus, it sense predominately pressure oscillations connected with cavitation cloud collapses, which appear in its vicinity.

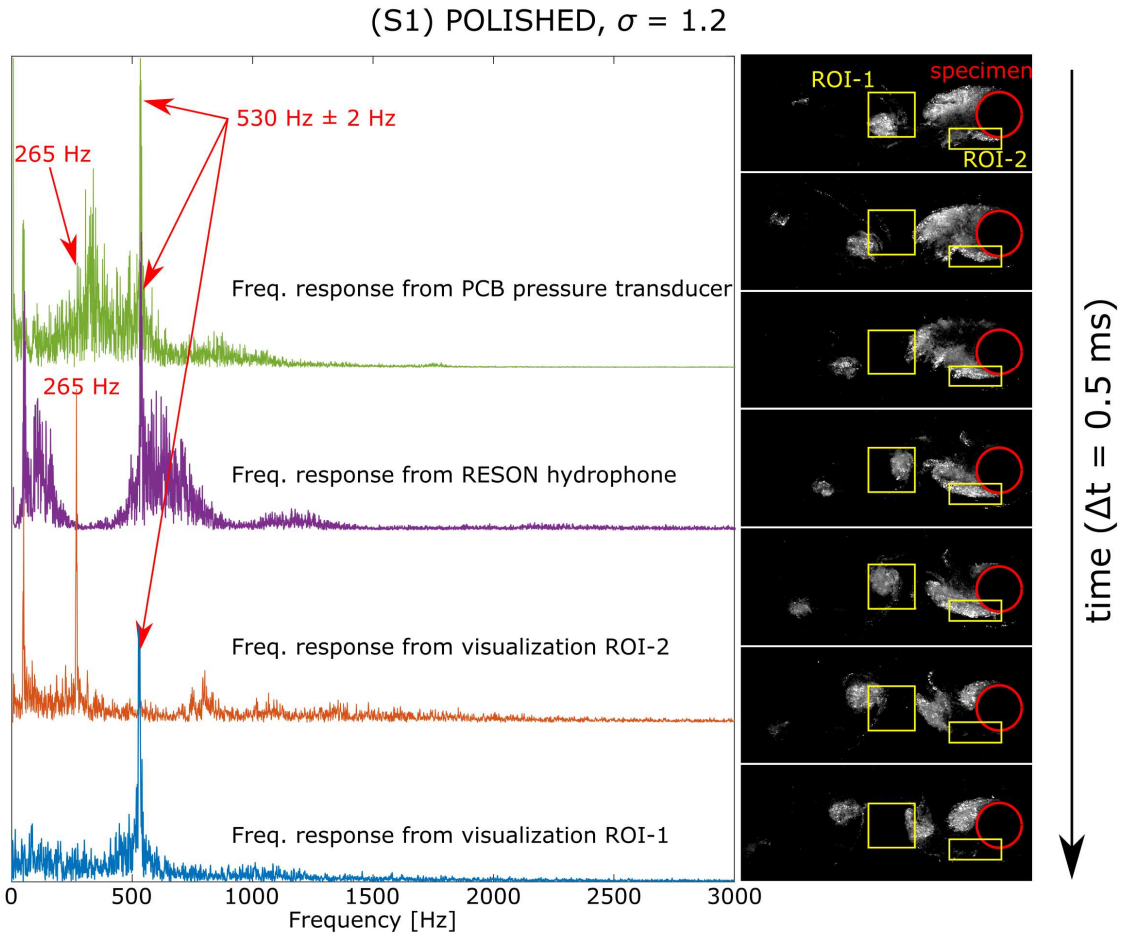

Figure S24. Frequency response, measured by different techniques for the polished sample S1 at $\sigma = 1.4$.

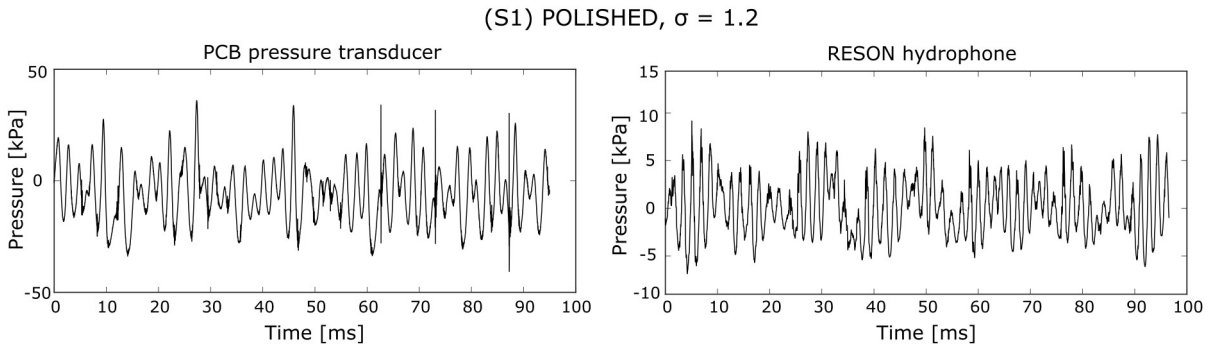

Figure S25. The pressure as a function of time, measured by hydrophone RESON (left) and PCB pressure transducer (right) for the polished sample S1 at $\sigma = 1.4$.

8 Evaluation of the frequency response

In order to compare the individual spectra between all the samples tested under different flow conditions, we have fitted the Gaussian function to the secondary peaks (as shown by the green line in Figure S26):

$$Y\ (f) = a\mathrm{e}^{-\frac{1}{2}\left(\frac{f-f_0}{\sigma_f}\right)^2} \tag{S14}$$

where σ_f stands for the standard deviation of the frequency distribution. It was used to calculate the standard deviation of the Strouhal numbers (the error bars in Figure 9 in the manuscript).

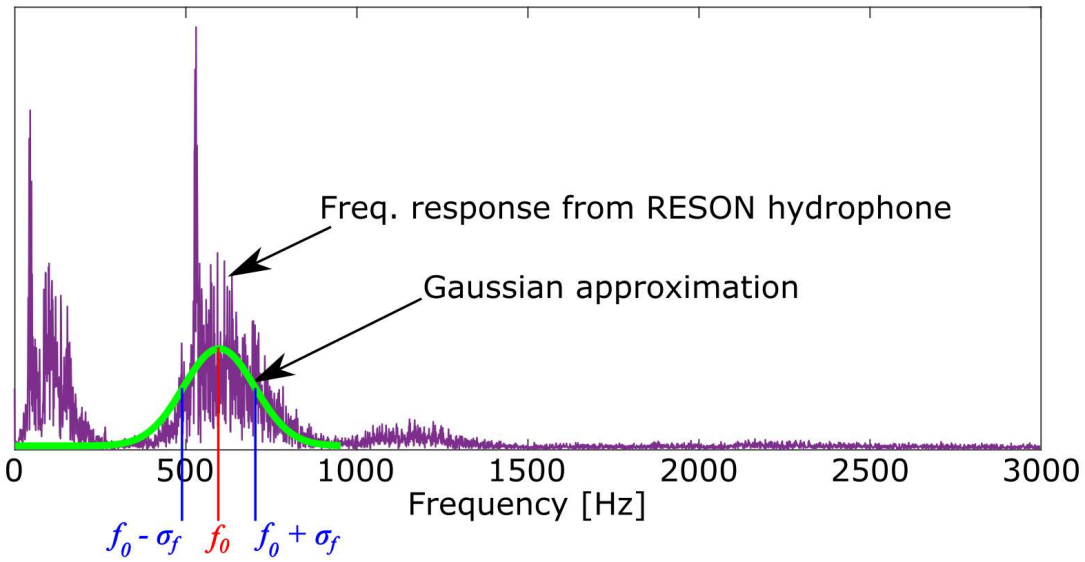

Figure S26. Fitting the Gaussian function on the FFT frequency spectrum, acquired by hydrophone RESON for polished sample S1 at $\sigma = 1.4$.